Hydrodynamic interactions between two spherical bubbles rising side by side in a viscous liquid

By DOMINIQUE LEGENDRE, JACQUES MAGNAUDET
AND GUILLAUME MOUGIN

Institut de Mécanique des Fluides de Toulouse, UMR CNRS/INPT/UPS 5502, 2, Allée Camille Soula, 31400 Toulouse, France

The three-dimensional flow past two identical spherical bubbles moving side by side in a viscous fluid is studied numerically by solving the full Navier–Stokes equations. The bubble surface is assumed to be clean so that the outer flow obeys a zero-shear-stress condition. The present study describes the interaction between the two bubbles over a wide range of Reynolds number ($0.02 \leqslant Re \leqslant 500$, Re being based on the bubble diameter and rise velocity), and separation S ($2.25 \leqslant S \leqslant 20$, S being the distance between the bubble centres normalized by the bubble radius). The flow structure, the vorticity field, the sign of the interaction force and the magnitude of the drag and lift forces are analysed; in particular the latter are compared with analytical expressions available in the potential flow limit and in the limit of low-but-finite Reynolds number. This study sheds light on the role of the vorticity generated at the bubble surface in the interaction process. When vorticity remains confined in a boundary layer whose thickness is small compared to the distance between the two bubbles, the interaction is dominated by the irrotational mechanism that results in an attractive transverse force. In contrast, when viscous effects are sufficiently large, the vorticity field about each bubble interacts with that existing about the other bubble, resulting in a repulsive transverse force. Computational results combined with available high-Reynolds-number theory provide empirical expressions for the drag and lift forces in the moderate-to-large Reynolds number regime. They show that the transverse force changes sign for a critical Reynolds number whose value depends on the separation. Using these computational results it is shown that, depending on their initial separation, freely moving bubbles may either reach a stable equilibrium separation or move apart from each other up to infinity.

1. Introduction

Bubbly flows with moderate-to-large bubble concentration (typically from a few per cent to 20% volume fraction) occur in many natural and industrial processes. However the current understanding of such flows and the predictive models used to describe their evolution are far from satisfactory because of the difficulty in describing direct hydrodynamic interactions between bubbles. Up to now, most of the numerical investigations devoted to finite-Reynolds-number flows about bubbles, drops or rigid particles have focused on the case of a single particle. While such investigations have provided important results concerning the drag, added-mass and shear-induced lift forces acting on an isolated particle (see e.g. Magnaudet & Eames

2000), applicability of these results to the description of dispersed flows is limited to low particle concentrations (typically less than 1–2%), since the hydrodynamic field about a particle moving close to other particles is modified by the presence of its neighbours. In particular, direct hydrodynamic interactions are expected to greatly influence the spatial distribution of the dispersed phase in flow regions where the particle concentration is significant. This is especially true for light particles and bubbles, since most of the inertia of the complete system then lies within the carrying fluid.

Hydrodynamic interactions between particles have been extensively studied in the context of creeping flow theory, particularly in order to determine the equivalent viscosity of the suspension (Batchelor 1971, 1972; Batchelor & Green 1972*a*,*b*; Hinch 1977). More recently, Stokesian dynamics (Durlofsky, Brady & Bossis 1987; Brady & Bossis 1988) has emerged as a powerful technique to compute the creeping flow generated by a large number of interacting particles. In the opposite limit of irrotational flow, several investigations based on the pioneering works of Jeffrey (1973) and van Wijngaarden (1976) have considered the interaction between two clean spherical bubbles (see e.g. Kok 1993*a* and references therein). Irrotational flow is generally regarded as a valid model for bubbly flows in which the bubble Reynolds number is large enough for the vorticity generated at the bubble surface to remain confined in a thin boundary layer and a thin wake. The aforementioned studies in which this assumption was used showed that when a pair of bubbles rises in a quiescent liquid due to buoyancy, the bubbles are attracted towards (resp. repelled from) each other when the angle between their line of centres and the vertical direction is in (resp. outside) the range $]\theta_c, 180° - \theta_c[$, θ_c being a critical angle ranging from 35° when the two bubbles are in contact to 54° when they are widely separated. These studies also established that the stable position of a pair of rising bubbles is reached when the two bubbles come in contact, their line of centres being perpendicular to the rise velocity (van Wijngaarden 1993). Irrotational flow theory was also used by several authors to compute the evolution of a suspension of bubbles. For instance, Sangani & Didwania (1993) and Smereka (1993) solved the *n*-body problem for a large collection of spherical bubbles moving under buoyancy in a periodic box. The most important conclusion of these 'direct' irrotational simulations is that bubbles tend to form horizontal clusters at large time, which is not unexpected considering the results mentioned above for a pair of bubbles. However this conclusion is at odds with observations, since a large number of experiments have shown that when a cloud of bubbles rises at moderate or large Reynolds number in a large batch of liquid otherwise at rest, the bubble distribution tends to be statistically homogeneous. This experimental trend has recently been confirmed by computations in which some hundreds of deformable bubbles rising at moderate Reynolds number (typically 10 to 30) evolve freely in a periodic box (Bunner & Tryggvason 2002). The most plausible explanation for this discrepancy with irrotational predictions is that potential flow theory has limited capabilities for describing some of the characteristics of flows about real bubbles whose rise Reynolds number is obviously finite, even though large. At low to moderate Reynolds number, viscous diffusion of vorticity produced at the bubble surface is significant and the assumption of irrotational flow is certainly irrelevant in a significant part of the liquid. Similarly one may expect that if the distance separating two bubbles becomes small enough, effects of vorticity cannot be neglected in the gap between them, whatever the Reynolds number. These arguments suggest that the irrotational description of bubbly flows has intrinsic limitations which are still to be understood.

Hydrodynamic interactions at finite Reynolds number were first explored by Oseen (1927) who considered some particular situations in which two rigid spheres interact in the presence of small-but-finite inertial effects (see §4). The corresponding solutions are obviously not directly applicable to drops and bubbles. Nevertheless the interesting point is that these solutions predict a repelling force for the case of two spheres settling side by side. A similar tendency was observed in the numerical simulations of Kim, Elgobashi & Sirignano (1993). They showed that two rigid spheres placed in a uniform stream perpendicular to their line of centres are attracted towards each other at large Reynolds number, while they are repelled when the Reynolds number is lower than a critical value depending on the separation distance. Similarly, Yuan & Prosperetti (1994) studied numerically the case of two bubbles rising in line at moderate-to-large Reynolds number. In contrast with the irrotational prediction according to which the two bubbles are repelled however large the distance that separates them, they showed that this separation reaches an equilibrium value corresponding to a balance between the inertial repulsion predicted by irrotational theory and an attractive wake effect due to the suction of the second bubble in the wake of the leading one. Finally, we note that in their full numerical simulations of the motion of a dozen of deformable buoyant bubbles rising in a periodic box, Esmaeeli & Tryggvason (1998, 1999) observed that the bubble distribution was more uniform at low Reynolds number ($Re \approx 1$–2) than at moderate Reynolds number ($Re \approx 20$–30) where a slight tendency for horizontal bubble pairs to form was noticed. They also observed that, compared with bubbles arranged in a regular array, freely evolving bubbles rise faster at low Reynolds number while they rise more slowly at moderate Reynolds number.

This brief review shows that finite-Reynolds-number effects may significantly change the structure and evolution of a bubbly flow. In order to clarify the key role of vorticity and the limitations of irrotational flow theory, numerical solutions of the full Navier–Stokes equations can be very helpful. As demonstrated by Bunner & Tryggvason (2002), it is now possible to compute the evolution of some hundreds of bubbles on a fixed numerical grid. Such computations widen horizons in that it becomes possible to follow the time-dependent evolution of a complex disordered system and to compute various statistics of interest. However, properly capturing thin boundary layers and wakes on such fixed grids is not easy, which is why available results obtained by these techniques are currently limited to Reynolds numbers of $O(10)$. Similarly, owing to the limited size of the computational box with respect to the bubble size, it is hard to capture accurately far-field effects which are crucially important in the low-but-finite Reynolds number regime at low concentration.

As is well known, provided one restricts the scope of the investigation to much simpler geometrical configurations, highly accurate results covering a wider range of Reynolds number can be obtained by using boundary-fitted grids. Results concerning the axisymmetric flow about two or more particles moving in line were, for instance, obtained by Tal, Lee & Sirignano (1984) for solid spheres and by Patnaik (1986), Raju & Sirignano (1990) and Chiang & Sirignano (1993) for droplets. As pointed out above, Yuan & Prosperetti (1994) considered the case of two bubbles rising in line. However, despite their intrinsic interest, their results have a limited bearing because the high-Reynolds-number, in-line configuration is known to be unstable to lateral perturbations, at least in pure liquids (Harper 1970, 1997; Kumaran & Koch 1993, Katz & Meneveau 1996). Indeed Kok (1993b) and Duineveld (1994) studied experimentally the evolution of two high-Reynolds-number bubbles rising in line in ultrapure water and confirmed that the pair of bubbles tends to rotate in order to line up horizontally. Hence it seems that the most important configuration to be
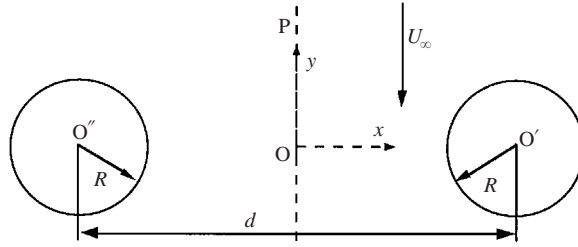
FIGURE 1. Sketch of the flow configuration and coordinate system.

studied in detail using a boundary-fitted technique is that where the two bubbles rise perpendicularly to their line of centres. To the best of our knowledge, the only detailed computations concerning this fully three-dimensional configuration are those of Kim *et al.* (1993) with two rigid spheres. In their study, the particle Reynolds number was varied between 50 and 150 and the distance between the two particle centres ranged from 3 to 50 particle radii.

The aim of the present study is to perform a similar investigation in the case of two clean spherical bubbles, i.e. two spheres under a shear-free condition instead of a no-slip one. The finite-Reynolds-number hydrodynamic interaction of two particles moving perpendicularly to their line of centres has several crucial consequences for the particle trajectories. In particular, the drag force is expected to be modified compared to the case of an isolated particle, and there is a transverse or lift force directed along the line of centres. We compute this flow past two bubbles by solving the full Navier–Stokes equations for Reynolds numbers (based on the bubble diameter and rise velocity) ranging from 0.02 to 500 and distances between the bubble centres ranging from 2.25 to 20 bubble radii in most cases. The paper is organized as follows. The governing equations of the problem and the associated dimensionless coefficients are given in §2. Section 3 is devoted to a short description of the most important numerical aspects and to several preliminary tests. In particular, extensive comparisons between high-Reynolds-number results and irrotational predictions are reported. In §4 we briefly derive analytical results for the hydrodynamic forces in the low-Reynolds-number limit, starting from the results of Vasseur & Cox (1977) for a pair of rigid spheres. The evolution of the velocity and vorticity fields with the separation distance and Reynolds number is described in §5. Section 6 is devoted to an extensive analysis of the numerical results obtained for the hydrodynamic forces acting on the bubbles. Concluding remarks are given in §7.

2. Statement of the problem

Let us consider a pair of spherical bubbles of radius R (figure 1) located at the respective positions $\boldsymbol{x} = -d/2\boldsymbol{e}_x$ and $\boldsymbol{x} = +d/2\boldsymbol{e}_x$ in a Cartesian frame of reference (x, y, z), the associated unit vectors being $(\boldsymbol{e}_x, \boldsymbol{e}_y, \boldsymbol{e}_z)$. The bubbles rise with a velocity $U_\infty \boldsymbol{e}_y$ in an unbounded Newtonian liquid at rest at infinity. Equivalently, we may study the problem of a pair of bubbles at rest in a uniform flow $\boldsymbol{U} = -U_\infty \boldsymbol{e}_y$. When the wake of the bubbles is stable (i.e. vortex shedding does not occur), the present problem is equivalent to that of a spherical bubble rising parallel to a symmetry plane (P in figure 1), and this problem is also symmetric with respect to the plane $z = 0$. Consequently, we only need to solve the governing equations in a quarter of the space, say $x \geqslant 0$ and $z \geqslant 0$. Denoting the velocity and pressure fields by $\boldsymbol{V}$

and P, respectively, the incompressible flow about the bubbles is governed by the Navier–Stokes equations

$$\left.\begin{aligned} \nabla \cdot V &= 0, \\ \frac{\partial V}{\partial t} + V \cdot \nabla V &= -\frac{1}{\rho}\nabla P + \nabla \cdot \tau, \end{aligned}\right\} \tag{1}$$

where $\tau = \nu(\nabla V + {}^{T}\nabla V)$ is the viscous part of the stress tensor $\Sigma = -PI + \rho\tau$, ρ and ν denoting the density and the kinematic viscosity of the liquid, respectively. The boundary condition far from the bubbles is

$$V \to -U_{\infty}e_{y} \quad \text{for} \quad r \to \infty, \tag{2}$$

where $r = \|x\|$ with $x = xe_{x} + ye_{y} + ze_{z}$. On the bubble surface the normal velocity must vanish, owing to impermeability. Moreover the dynamic viscosity of the gas filling the bubble is generally negligibly small compared to that of the surrounding liquid. If we assume in addition that the bubble surface is clean, i.e. free of any surfactant or contaminant, the matching of the shear stresses across the bubble surface reduces to a shear-free boundary condition for the liquid. Hence the boundary conditions at the bubble surface are

$$\left.\begin{aligned} V \cdot n &= 0 \\ n \times (\tau \cdot n) &= 0 \end{aligned}\right\} \quad \text{for} \quad r = R, \tag{3}$$

where $n = x/\|x\|$ is the outward unit normal to the bubble surface.

The steady solution of the problem depends upon two characteristic parameters, namely the Reynolds number Re and the non-dimensional distance S, defined as

$$Re = \frac{2RU_{\infty}}{\nu}, \quad S = \frac{d}{R}. \tag{4}$$

In the present work Re is varied between 0.02 and 500 and most of the computations concern separations ranging from $S = 2.25$ to 20 (note that $S = 3$ corresponds to a pair of bubbles separated by a gap of one bubble radius, whereas the case of two bubbles in contact corresponds to $S = 2$). Clearly, the assumption that the bubbles remain spherical implies that the Weber number $We = 2\rho RU_{\infty}^{2}/\sigma$ (σ being the surface tension) is small compared to unity. In a high-surface-tension liquid like pure water, it appears reasonable to neglect the deformation resulting from non-zero Weber-number effects up to Reynolds numbers about 250.

As stated in the introduction, we are particularly interested in obtaining the total force acting on the bubble. This force may be split into its drag component F_{D} (i.e. its component antiparallel to e_{y}), and its lift or transverse component F_{L} parallel to e_{x}. We thus define

$$F_{L} = e_{x} \cdot \int_{\Gamma} \Sigma \cdot n \, d\Gamma, \quad F_{D} = -e_{y} \cdot \int_{\Gamma} \Sigma \cdot n \, d\Gamma, \tag{5}$$

where Γ denotes the bubble surface. The results concerning these forces will be expressed in terms of the dimensionless lift and drag coefficients C_{L} and C_{D} obtained by dividing the corresponding component of the force by $\pi R^{2}\rho U_{\infty}^{2}/2$. Moreover we shall sometimes separate the contribution due to pressure effects from that due to the normal viscous stress. Hence the lift coefficient will be split into the pressure contribution C_{Lp} and the viscous contribution $C_{L\mu}$. Note that in the subdomain $x \geqslant 0$, a negative (resp. positive) value of the lift coefficient corresponds to an attractive (resp. repulsive) force.

3. Numerical method and tests

3.1. *The JADIM code*

The computations reported below were carried out with the JADIM code described in previous publications (Magnaudet, Rivero & Fabre 1995; Calmet & Magnaudet 1997; Legendre & Magnaudet 1998). This code solves the three-dimensional unsteady Navier–Stokes equations written in velocity–pressure variables in a general system of orthogonal curvilinear coordinates. The discretization makes use of a staggered mesh and the equations are integrated in space using a finite volume method with second-order accuracy, all spatial derivatives being approximated using second-order centred schemes. Time advancement is achieved through a Runge–Kutta/Crank–Nicolson algorithm which is second-order accurate in time, while incompressibility is satisfied at the end of each time step by solving a Poisson equation for an auxiliary potential. A point to be noted is that the computational grids used here (cf. § 3.2 and figure 2) are highly curved near the bubble. Thus the curvilinear source terms involved in the momentum equations have a significant influence in these regions, which makes a correct discretization of these terms crucial for the accuracy of the results. To reach this goal, a specific procedure allowing us to ensure that these curvilinear terms do not create artificial sinks or sources of momentum in the discrete equations is used (see Legendre & Magnaudet 1998).

3.2. *The orthogonal grid*

Most of the previous studies dealing with the interaction of two droplets or particles solved the Navier–Stokes equations in a non-orthogonal coordinate system. We prefer to use orthogonal coordinates because this choice reduces the number of additional terms involved in the momentum equations and makes the prescription of boundary conditions (3) straightforward. Moreover, accuracy is more easily guaranteed when the coordinate lines are orthogonal. For the problem considered here, such a coordinate system may be obtained by using bispherical coordinates, as employed by Yuan & Prosperetti (1994). However, the corresponding coordinate lines do not form an outer boundary with a smooth and simple shape, making the far-field boundary conditions difficult to impose.

We tried several different grid systems, including that obtained by rotating about the x-axis the two-dimensional grid built on the streamlines $\eta = \mathrm{const.}$ and the equipotential lines $\xi = \mathrm{const.}$ of the potential flow around a cylinder located near a plane (Milne–Thomson 1968, p. 185). It turned out that obtaining grid-independent results in both low- and high-Reynolds-number situations with this type of grid was quite difficult. Consequently we moved to the grid system shown in figure 2. A plane grid is first obtained by inverting the equations defining the streamlines $\eta = \mathrm{const.}$ and the equipotential lines $\xi = \mathrm{const.}$ of the potential flow generated by two circular cylinders moving in line along the x-axis. Then the three-dimensional grid is generated by rotating the plane grid about the x-axis with an angle ϕ. The (ξ, η, ϕ) grid used in the computations reported below is made of $(N + N_b + N_\xi) \times N_\eta \times N_\phi$ nodes (figure 3). Here N is the number of nodes located between the bubble and the symmetry plane $x = 0$, N_b is the number of nodes describing one half of the circumference of the bubble (from $x = d/2 - R$ to $x = d/2 + R$), N_ξ is the number of nodes between the bubble and the outer boundary in the x-direction, while N_η and N_ϕ are the number of nodes along the radial (y) and azimuthal (ϕ) directions, respectively (keep in mind that ϕ varies only from zero to π because the flow is symmetric with respect to the plane $z = 0$). The bubble surface is thus discretized with $N_b \times N_\phi$ nodes in the ξ- and ϕ-directions. The outer boundary of the computational domain is a circular cylinder
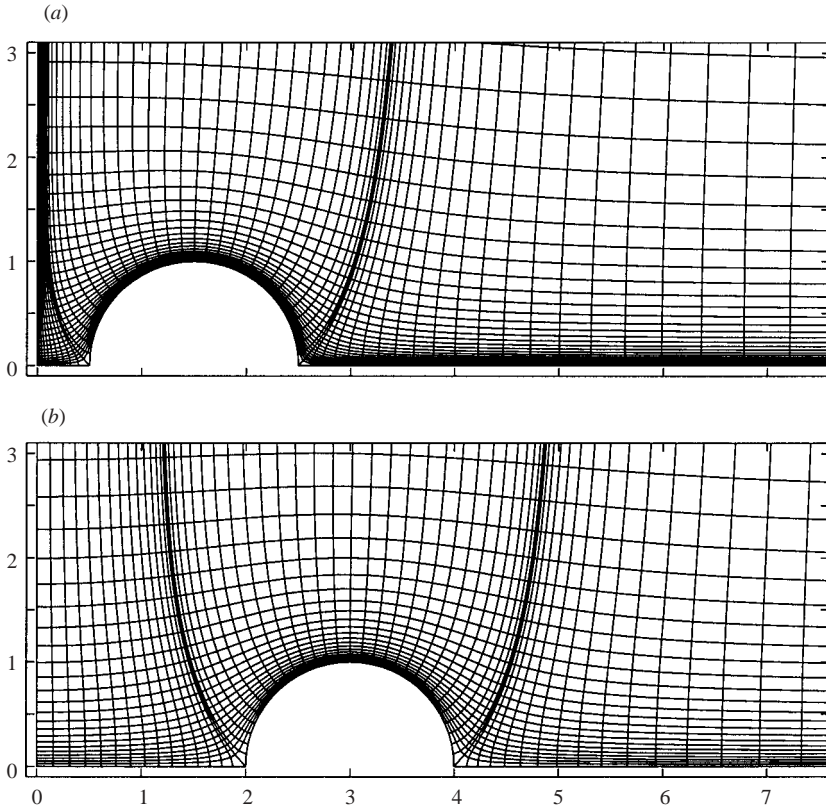
(*a*)

(*b*)

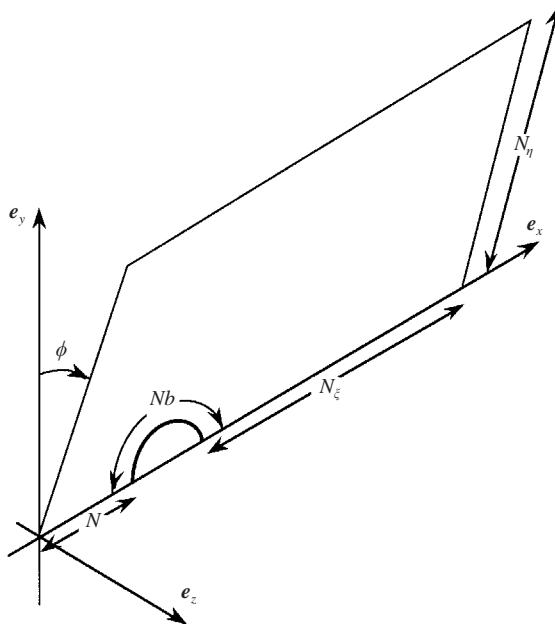FIGURE 2. Partial view of the grid near the bubble. (*a*) $S = 3$, (*b*) $S = 6$.

FIGURE 3. Definition of the number of nodes in the computational domain.

		$Re = 0.1$		$Re = 300$	
(a)	N	C_D	C_L	C_D	C_L
	5	140.3	0.708	0.147	-0.0666
	8	140.2	0.709	0.147	-0.0659
	10	140.2	0.709	0.147	-0.0657
	12	140.2	0.709	0.147	-0.0656
	15	140.2	0.708	0.147	-0.0656
(b)	N_b	C_D	C_L	C_D	C_L
	24	139.1	0.691	0.148	-0.0667
	28	140.1	0.710	0.148	-0.0655
	30	140.2	0.709	0.147	-0.0657
	36	140.5	0.709	0.147	-0.0649
	40			0.147	-0.0649
(c)	N_ϕ	C_D	C_L	C_D	C_L
	16	140.1	0.703	0.149	-0.0663
	24	140.2	0.708	0.147	-0.0658
	32	140.2	0.709	0.147	-0.0657
	48	140.3	0.708	0.147	-0.0657
(d)	R_∞/R	C_D	C_L	C_D	C_L
	20			0.147	-0.0656
	40			0.147	-0.0657
	60	141.2	0.729	0.147	-0.0656
	80	140.2	0.709	0.147	-0.0656
	100	139.8	0.709		

TABLE 1. Effect of the number of nodes on the drag and lift forces: (*a*) varying the number of nodes N between the bubble and the symmetry plane ($S = 3$, $N_b = 30$, $N_\phi = 32$, $R_\infty/R = 80$, $\delta/R = 0.01$); (*b*) varying the number of nodes N_b describing the bubble surface ($S = 3$, $N = 10$, $N_\phi = 32$, $R_\infty/R = 80$, $\delta/R = 0.01$); (*c*) varying the number of nodes N_ϕ in the azimuthal direction ($S = 3$, $N = 10$, $N_b = 30$, $R_\infty/R = 80$, $\delta/R = 0.01$); (*d*) varying the size R_∞/R (thus the numbers of nodes N_ξ and N_η) of the computational domain ($S = 3$, $N = 10$, $N_b = 30$, $N_\phi = 32$, $\delta/R = 0.01$).

of radius R_∞ and height $R_\infty + d/2$. Clearly, N_ξ and N_η directly depend on R_∞ and on the distribution of nodes between the bubble and the outer boundary. A constant spacing is used in the ϕ-direction. In the ξ- and η-directions, we select a geometrical distribution of nodes ensuring that the length ratio between two successive cells is less than 1.15 everywhere in the numerical plane (ξ, η). Nevertheless, owing to the singularity of the mapping $(\xi, \eta) \rightarrow (x, y)$ near the poles of the bubble, the length ratio in the physical plane (x, y) may exceed this value near the iso-ξ lines issuing from the poles, as may be seen in figure 2. We have already used such mappings in some of our previous studies (Magnaudet *et al.* 1995; Legendre & Magnaudet 1998) and found that the somewhat large length ratio between two successive cells encountered in this sub-region does not affect the overal accuracy of the calculations. We tested different numbers of nodes (N, N_b, N_ϕ) and domain sizes R_∞ for each separation distance S and analysed the effects of these parameters on the the drag and lift forces. As a typical example, we report these effects for $S = 3$ in table 1 for both low ($Re = 0.1$) and high ($Re = 300$) Reynolds number. The results clearly show that increasing the number of nodes and the size of the computational domain yields grid-independent results. As is well known, the smaller the Reynolds number, the larger the artificial confinement

δ/R	$Re = 0.1$		$Re = 300$	
	C_D	C_L	C_D	C_L
0.0015			0.147	−0.0664
0.002			0.147	−0.0657
0.004			0.148	−0.0630
0.01	140.2	0.709	0.151	−0.0580
0.015	140,2	0.708		
0.02	140.2	0.712		
0.04	140.3	0.686		

TABLE 2. Effect of the relative size δ/R of the cells located at the intersection of the x-axis and the bubble surface ($S = 3$, $N = 10$, $N_b = 30$, $N_\phi = 32$, $R_\infty/R = 80$).

effects. Hence we selected $R_\infty/R = 100$ for $Re \leqslant 0.1$, $R_\infty/R = 80$ for $0.1 < Re \leqslant 20$ and $R_\infty/R = 40$ for larger Reynolds numbers.

Another point to be considered in detail is the effect of the distance δ from the bubble surface to the first node above it near the singular points $x = d/2 \pm R$ of the x-axis. This parameter was found to be crucial for an accurate description of the interaction force in the high-Reynolds-number regime, owing to the low magnitude of this force for most values of S. The reason for this is twofold. First, the grid is not symmetrical with respect to the plane $x = d/2$ parallel to the symmetry plane $x = 0$ and containing the bubble centre. Therefore numerical errors necessarily induce an artificial transverse force. Moreover the two cells located near the poles of the bubble, i.e. at the intersection of the x-axis and the bubble surface, are larger than those that cover the bubble surface elsewhere (especially in the plane $x = d/2$) and are non-orthogonal, thus inducing some inaccuracy in the momentum balance. Hence reducing δ allows us to reduce both sources of error. According to the results of the tests reported in table 2, δ/R was set to 0.002 for $Re \geqslant 10$ and to 0.01 for $Re < 10$. For instance, figure 2(a) corresponds to a grid with $\delta/R = 0.002$ while figure 2(b) corresponds to $\delta/R = 0.01$.

Finally, we found that the numerical results are not very sensitive to the numbers of nodes N_ϕ and N (tables 1a and 1d). Consequently we selected $N_\phi = 32$ in all the computations and increased N regularly with the distance $d/2$ between the bubble and the symmetry plane. More precisely, the computations reported below were carried out with $N = 5$ for $S \leqslant 2.5$, $N = 10$ for $3 \leqslant S \leqslant 4$, $N = 15$ for $5 \leqslant S \leqslant 10$ and $N = 20$ for $S > 10$.

3.3. *Preliminary tests*

The capability of the JADIM code to describe accurately three-dimensional flows about bubbles and rigid particles has already been proved (see e.g. Legendre & Magnaudet 1998). Consequently we mainly checked the effects of the grid described above. In a first series of tests we computed the flow field in situations where the relative distance S between the two bubbles is much larger than unity ($S = 80$ for $Re < 20$ and $S = 40$ for $Re > 20$). The lift force must then be almost zero and the drag force must correspond to that experienced by a single bubble rising in an unbounded fluid. This test was carried out for several Reynolds numbers ranging from 0.1 to 300. The values of the drag coefficient were compared with those obtained in our previous studies (Legendre & Magnaudet 1998) and with the general correlation proposed by

	$Re = 0.1$	$Re = 1$	$Re = 10$	$Re = 300$
This study, $S \gg 1$	161.9	17.4	2.48	0.141
Legendre & Magnaudet (1998)	162.2	17.4	2.43	0.141
Mei *et al.* (1994)	161.9	17.6	2.48	0.139

TABLE 3. Drag and lift coefficients for $S \gg 1$.

Mei, Klausner & Lawrence (1994), namely

$$C_D = \frac{16}{Re} \left\{ 1 + \left[\frac{8}{Re} + \frac{1}{2} \left(1 + \frac{3.315}{Re^{-1/2}} \right) \right]^{-1} \right\}. \tag{6}$$

The results are shown in table 3. The difference between results from (6) and our previous results is less than 1% for all values of Re while the lift force is of the order of the round-off error. As (6) tends towards Moore's (1963) and Taylor & Acrivos' (1964) asymptotic results in the limit of large and small Re, respectively, we conclude that our numerical predictions for the drag force in the limit of large separations agree well with known theoretical results.

3.4. *Tests in irrotational flow*

Solutions for the velocity potential of two spheres of identical radius moving at an arbitrary angle with respect to their line of centres have been obtained by Miloh (1977) and Biesheuvel & van Wijngaarden (1982), using earlier results by Jeffrey (1973) and van Wijngaarden (1976). Once the velocity potential is known, the kinetic energy may be evaluated and the equations of motion can be obtained though Lagrange's formalism. Following van Wijngaarden (1976), the lift coefficient C_L is then found in the form of an infinite series whose first terms are

$$C_L = -6S^{-4} \left(1 + S^{-3} + \tfrac{16}{3} S^{-5} + \tfrac{3}{4} S^{-6} + 15 S^{-7} + \tfrac{22}{3} S^{-8} + \tfrac{65}{2} S^{-9} + \tfrac{767}{9} S^{-10} + O(S^{-11}) \right). \tag{7}$$

For the flow configuration considered here, this lift coefficient is always negative, thus corresponding to an attractive force. This is because quadrupoles and higher-order singularities involved in the multipole expansion of the velocity potential combine in such a way that the downward fluid velocity is larger between the two bubbles than in the exterior fluid, thus inducing a pressure gradient directed away from the symmetry plane $x = 0$. It is worth noting that the series giving C_L converges rapidly for moderate or large separations, typically $S \geqslant 3$. For instance the term proportional to S^{-14} contributes less than 0.1% of the total value of C_L for $S = 3$. In contrast, this term still contributes about 8% of the value of C_L for $S = 2$ and a correct estimate of C_L then requires more than one hundred terms. The modification of the viscous drag force due to the hydrodynamic interaction between the two bubbles was evaluated by Kok (1993a), using a global kinetic energy balance 'à la Levich' (Levich 1962, pp. 444–445). In this approach the flow is assumed to be irrotational everywhere except right at the surface of the bubbles where the shear-free condition generates an infinitely thin vortex sheet. For two bubbles rising side by side, Kok (1993a) obtained

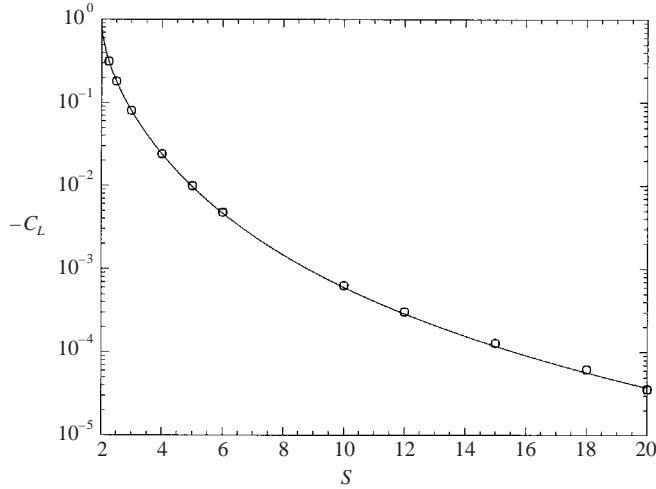$$C_D = \frac{48}{Re}(1 + g(S)) + O(Re^{-3/2}), \tag{8}$$

FIGURE 4. Lift coefficient in the potential flow limit. $\circ$, $Re = 1$; $\square$, $Re = 300$;
——, equation (7).

with

$$g(S) = S^{-3} + \tfrac{3}{4}S^{-6} + \tfrac{11}{3}S^{-8} + \tfrac{1}{2}S^{-9} + \tfrac{39}{4}S^{-10} + O(S^{-11}).$$

Hence, compared to the unbounded case, corrections due to the presence of the second bubble tend to increase the drag force. This is because the interaction results in a higher strain rate in the fluid located between the two bubbles.

We checked our code against predictions (7) and (8). For this purpose we considered the results obtained during the first time steps after the flow has being initialized with a uniform velocity profile far upstream. As vorticity is generated at the bubble surface by the shear-free condition and is then diffused in the boundary layer and shed in the wake, its influence is expected to be negligible during the very first time steps (typically over a period of time T such that $T \ll R^2/\nu$). Indeed, for $t = O(T)$, we observed quasi-constant values of the drag and lift coefficients. As shown in figure 4, the corresponding numerical values of C_L follow closely the analytical prediction (the analytical value was calculated by considering 135 terms in the infinite series (7)). The difference is less than 2.5% up to $S = 6$ and increases up to 8% for $S = 20$. This difference increases with the separation because the magnitude of the lift force decreases quickly with S and becomes of the order of the numerical error for large S. For instance, the magnitude of the lift force corresponding to $S = 20$ is only about 0.02% of the magnitude of the drag force. The drag increase due to the presence of the second bubble is compared with the analytical prediction (8) in figure 5. The agreement is found to be satisfactory up to $S = 5$ and deteriorates for larger separations, owing to the smallness of the effect under consideration. These comparisons demonstrate the ability of our code to capture properly the irrotational mechanisms of interaction, even in situations where the resulting effects are much weaker than the leading-order drag force. Given the above results, we are confident that the transverse force is accurately predicted, even when the lift coefficient is as small as 10^{-4} ($S \approx 17$), whereas relative modifications to the drag force of $O(10^{-2})$ or more are also correctly reproduced.

To complete this series of tests, we considered the added-mass force acting on the pair of bubbles when the free-stream velocity $-U_\infty \boldsymbol{e}_y$ varies in time. It is well known
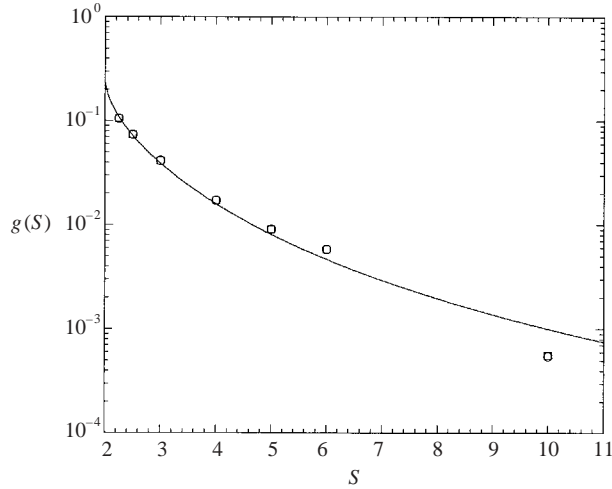
FIGURE 5. Relative drag increase due to the interaction in the potential flow limit.
○, $Re = 1$; □, $Re = 300$; ——, equation (8).

that if the flow were inviscid, the total force on each bubble would then reduce to the inertial force

$$\boldsymbol{F}_I = -\tfrac{4}{3}\rho\pi R^3(1 + C_M(S))\frac{\mathrm{d}U_\infty}{\mathrm{d}t}\boldsymbol{e}_y, \qquad (9)$$

C_M being the so-called added-mass coefficient (Batchelor 1967, p. 409). The first contribution in the right-hand side of (9) represents the force exerted by the outer flow on the volume of fluid occupied by the bubble. The second part is the added-mass force which arises because the presence of the bubble induces an acceleration of the surrounding fluid. In the past decade, theoretical and numerical investigations have demonstrated that the inertial force experienced by a spherical particle of arbitrary nature (i.e. a rigid particle, a drop or a bubble) moving in an unbounded flow is left unaltered by finite-Reynolds-number effects, the value of C_M then being $1/2$ whatever the relative strength of viscous effects and temporal acceleration compared to those of advection (see Magnaudet & Eames 2000 for a review). In other words, the contribution to the total force $\boldsymbol{F}(t)$ acting on the particle that depends directly on the instantaneous value of the acceleration $\mathrm{d}U_\infty(t)/\mathrm{d}t$ is identical to that predicted by irrotational theory. A mathematical argument explaining the reason for this may be found in a recent paper by Mougin & Magnaudet (2002a). Even though this result was obtained in an unbounded flow, the argument is more general. Hence in the present situation we expect to find an inertial force of the form (9) with $C_M(S)$ as predicted by irrotational theory, namely (van Wijngaarden 1976; Kok 1993a)

$$C_M(S) = \tfrac{1}{2}\left[1 + \tfrac{3}{2}S^{-3} + \tfrac{3}{4}S^{-6} + 3S^{-8} + \tfrac{3}{8}S^{-9} + \tfrac{27}{4}S^{-10}\right] + o(S^{-11}). \qquad (10)$$

For finite values of S the added-mass coefficient (10) is larger than that of a single sphere because the flow located between the two spheres experiences a larger acceleration compared to the unbounded case. To evaluate the inertial force numerically, we employed the procedure proposed by Rivero, Magnaudet & Fabre (1991). Briefly, this procedure consists in determining the inertial force at a given time t_1 through the difference between the total force obtained in two different situations. In the first of these, the accelerated flow is computed up to time $t_1 + \Delta t$ and the hydrodynamic

(a)	Re	0.1	1	10	50	100	300
	C_M	0.5503	0.5504	0.5502	0.5502	0.5502	0.5502
(b)	Ac	0.1	1	10	100	1000	
	C_M	0.5491	0.5502	0.5502	0.5502	0.5502	

TABLE 4. Influence of the Reynolds number and acceleration parameter on the added-mass coefficient C_M. (a) $S = 2.5$, $Ac = 100$, varying Re; (b) $S = 2.5$, $Re = 300$, varying Ac.
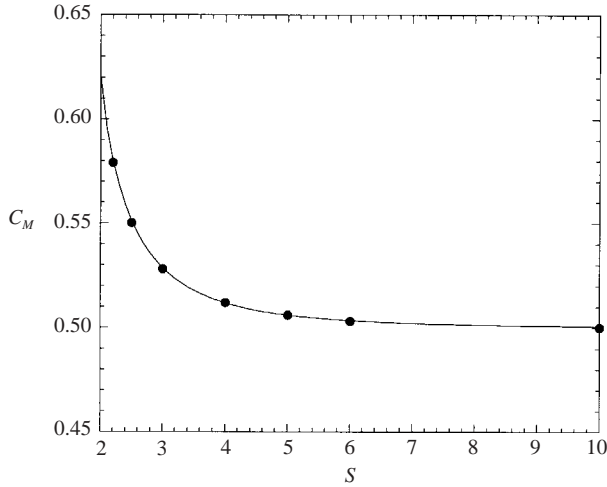

FIGURE 6. Added-mass coefficient C_M: ●, numerical values; —— equation (10).

force $\boldsymbol{F}(t_1 + \Delta t)$ is evaluated. In the second computation, the acceleration is set to zero at $t = t_1$ and the corresponding total force at time $t_1 + \Delta t$, say $\boldsymbol{F}'(t_1 + \Delta t)$, is evaluated. It can then be proved (see Rivero *et al.* 1991) that the difference $\boldsymbol{F} - \boldsymbol{F}'$ tends to $\boldsymbol{F}_I(t_1)$ in the limit $\Delta t \rightarrow 0$. We applied this method to the case where the free-stream velocity varies linearly in time, i.e. $U(t) = U_0 + \alpha t$, where α is a constant acceleration. We observed that for a given separation S, the variations of the added-mass coefficient with the acceleration parameter $Ac(t) = 2R\alpha/U_\infty^2(t)$ and Reynolds number $Re(t) = 2RU_\infty(t)/\nu$ were less than 0.2% (an example of these variations is given in table 4). These results confirm that added-mass effects are not altered by viscous effects, even in a bounded flow domain. Figure 6 shows the added-mass coefficient as a function of the dimensionless separation S. The numerical values are compared with the analytical prediction (10). The difference is found to be less than 1% for all separations. As shown by figure 6, the added-mass coefficient rapidly decreases as S increases, the difference with the value 1/2 for an unbounded flow being less than 1.2% for $S = 5$. We finally examined the influence of the acceleration on the transverse force. According to (9), the inertial force only contributes to the drag, so that over a short period of time the transverse force should not be altered when the flow is accelerated. Figure 7 compares the lift coefficient measured in an accelerating flow with that measured in a steady flow for the same values of the separation S and Reynolds number Re. The difference is less than 0.8% in all cases, confirming that no spurious transverse force is created by the code.
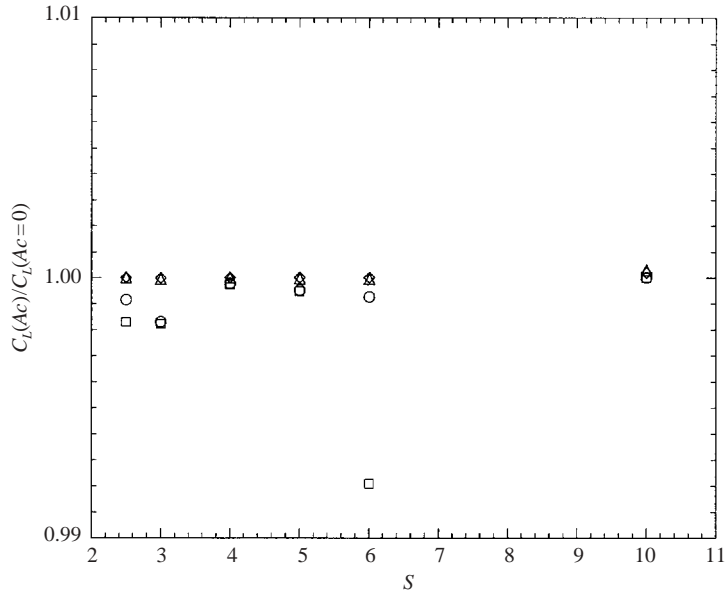
FIGURE 7. Effect of the acceleration on the transverse force. $\bigcirc$, $Ac = 100$, $Re = 300$;
$\square$, $Ac = 100$, $Re = 1$; $\triangle$, $Ac = 1$, $Re = 300$; $\diamond$, $Ac = 1$, $Re = 1$.

4. Asymptotic solutions in the low-Reynolds-number regime

Before we examine the results of the computations at finite Reynolds number, a discussion of asymptotic results that may be derived in the low-Reynolds-number limit is in order, as these results will help in understanding the evolution of hydrodynamical effects with the Reynolds number and will provide additional indications concerning the accuracy of the numerical procedure.

The problem of two rigid spheres settling side by side in a stagnant viscous fluid in the presence of small-but-finite Reynolds number effects was first examined by Oseen (1927) (see Happel & Brenner 1973, p. 282). Using a somewhat *ad hoc* approach based on the Oseen equation, he was able to obtain an expression for the interaction force and drag correction due to the presence of the second particle in the limit $Re \ll 1$, $ReS \gg 1$. The constraint $ReS \gg 1$ is satisfied when each particle lies in the outer (Oseen) region of the disturbance produced by the other particle, viscous effects and inertia then having a comparable magnitude in the region located near the symmetry plane of the flow. This problem was later revisited by Vasseur & Cox (1977) using the more rational and now familiar approach of matched asymptotic expansions. It is straightforward to extend the result of Vasseur & Cox to the case of a pair of bubbles. For this purpose let us start by noting that in the low-Reynolds-number regime, the force acting on a spherical drop of radius R and dynamic viscosity μ_I moving in a fluid of dynamic viscosity μ having a uniform velocity $\boldsymbol{u}$ far upstream is, in dimensional form,

$$\boldsymbol{F} = 4\pi R_\mu \mu R \boldsymbol{u} \quad \text{with} \quad R_\mu = \frac{2 + 3\mu_I/\mu}{2(1 + \mu_I/\mu)}. \tag{11}$$

This is the well-known Hadamard–Rybczynski formula (Clift, Grace & Weber 1978, p. 33). This formula can be used to obtain the $O(Re)$ approximation of the hydrodynamic force experienced by each particle by setting $\boldsymbol{u} = -U_\infty \boldsymbol{e}_y + \boldsymbol{u}_P$, U_∞ being the

rise/settling velocity of the particle and $\boldsymbol{u}_P$ a constant $O(Re)$ velocity correction due to the far-field disturbance produced by the presence of the two particles and their interaction. When the two particles are sufficiently far apart, the leading-order disturbance they induce in the far field can be obtained by replacing them by two point forces of strength $\boldsymbol{f} = 4\pi R_\mu \rho \nu R U_\infty \boldsymbol{e}_y$ located at the particle centres, i.e. $x = \pm d/2$, $y = z = 0$. In other words, the leading-order correction to the far-field velocity is due to the Stokeslet associated with each particle. As the governing equations for the leading-order disturbance in the far field are nothing but the Oseen equations, they are linear with respect to both the forcing term $\boldsymbol{f}$ and the velocity disturbance itself. Hence it turns out that $\boldsymbol{u}_P$ is directly proportional to $\boldsymbol{f}$, i.e. to the numerical factor R_μ. Coming back to (11) in which R_μ is again involved, we conclude immediately that, while the Stokes drag corresponding to vanishingly small Reynolds number ($Re \to 0$) and very large separation ($S \to \infty$) is just $\boldsymbol{F}_S = -4\pi R_\mu \rho \nu R U_\infty \boldsymbol{e}_y$, the leading-order correction due to finite inertial and interaction effects is proportional to R_μ^2. Using this argument, equations (9.24)–(9.26) of Vasseur & Cox (1977), originally derived for two rigid spheres ($R_\mu = 3/2$), yield immediately the drag and lift forces acting on two bubbles of vanishingly small viscosity ($R_\mu = 1$) rising side by side as

$$C_D(Re, Re\,S) = \frac{16}{Re}\left[1 + \frac{Re}{8} - \frac{1}{2}\frac{\mathrm{e}^{-Re\,S/4}}{S}\right], \tag{12a}$$

$$C_L(Re, Re\,S) = \frac{32}{Re^2\,S^2}\left[1 - \left(1 + \frac{Re\,S}{4}\right)\mathrm{e}^{-Re\,S/4}\right]. \tag{12b}$$

In contrast with the irrotational prediction (7), the lift coefficient is now positive for all values of $Re\,S$, indicating that the two bubbles are repelled from each other. Similarly, the interaction is found to decrease the drag force, whereas (8) indicates an opposite effect in the irrotational limit. As will become clear later, these behaviours, which are at odds with irrotational predictions, are due to the vorticity generated by the shear-free condition at the bubble surface. The term $Re/8$ in (12a) is the counterpart of the well-known Oseen correction $3Re/16$ for a rigid sphere (Taylor & Acrivos 1964). We can formally examine expressions (12) in the limit $Re\,S \to 0$, i.e. in the limit case where the distance between the two bubbles becomes small compared to the dimensionless Oseen radius Re^{-1}. We then obtain

$$C_D = \frac{16}{Re}\left[1 - \frac{1}{2S}\right] + O(1), \quad C_L = 1 + O(Re\,S). \tag{13a,b}$$

Hence the leading contribution to the lift coefficient becomes constant in this limit. More accurate results can be derived in the complementary case $S \gg 1$, $Re\,S \ll 1$ (i.e. when the second bubble lies in the inner (Stokes) region of the disturbance due to the first one) by considering higher-order contributions in the multipole expansion of the velocity field. This asymptotic limit is examined in the Appendix. In particular (A 5) shows that in the limit $Re \to 0$ the drag coefficient is then

$$C_D = \frac{16}{Re}\left(1 + \frac{1}{2S}\right)^{-1}. \tag{14a}$$

Furthermore, using techniques similar to those employed by Magnaudet, Takagi & Legendre (2003), we show (see A 11) that the lift coefficient is in this limit
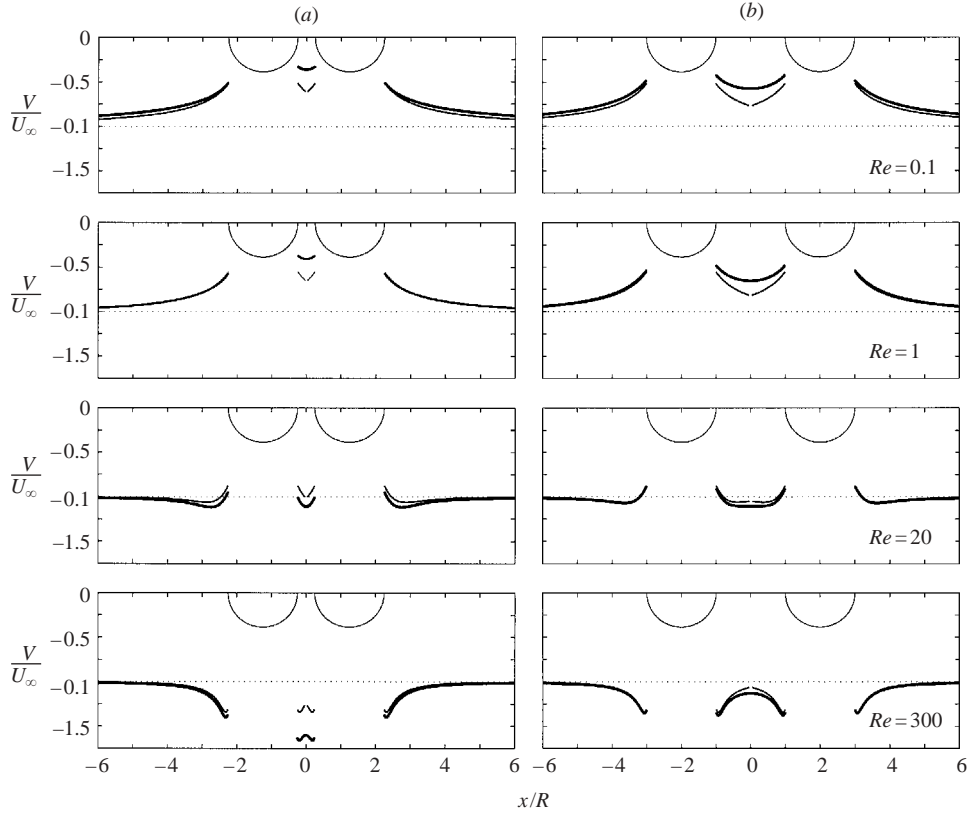
$$C_L = 1 + O(S^{-2}). \tag{14b}$$

FIGURE 8. Distribution of the vertical velocity V/U_∞ in the equatorial plane ($y=0$) of the bubble: ———, numerical profile: ———, numerical profile corresponding to an isolated bubble; ·····, $V/U_\infty = -1$. (a) $S = 2.5$; (b) $S = 4$.

Then (13a) appears to match the first-order expansion of (14a) in the limit of large separations, whereas the leading-order value of the lift coefficient in (14b) matches that given in (13b).

5. The velocity and vorticity fields

Figure 8 shows the computed profiles of the vertical velocity in the equatorial plane of the bubbles ($y=0$) for two different dimensionless separations ($S=2.5$ and 4) and for a wide range of Reynolds number. At high Reynolds number ($Re = 300$) these profiles clearly show the increased velocity that occurs in the gap $x \in [-d/2 + R, d/2 - R]$ and results in a pressure gradient directed away from the symmetry plane. The boundary layer can be distinctly seen on both sides of the bubble. When the Reynolds number decreases ($Re = 20$), the flow in the gap slows down and the velocity profile reaches its minimum on the bubble surface. At small enough Reynolds number ($Re = 1$ or 0.1), a blocking effect appears in the gap since the vertical velocity becomes smaller there than at any point of the $y=0$ plane located outside the gap. For instance the velocity at the point $(d/2 - R, 0, 0)$ on the bubble surface is about $0.33U_\infty$ for $S = 2.5$ at $Re = 0.1$ (resp. $0.42U_\infty$ for $S = 4$), while it is about $0.51U_\infty$ at the same Reynolds number for an isolated bubble (Legendre & Magnaudet 1998).
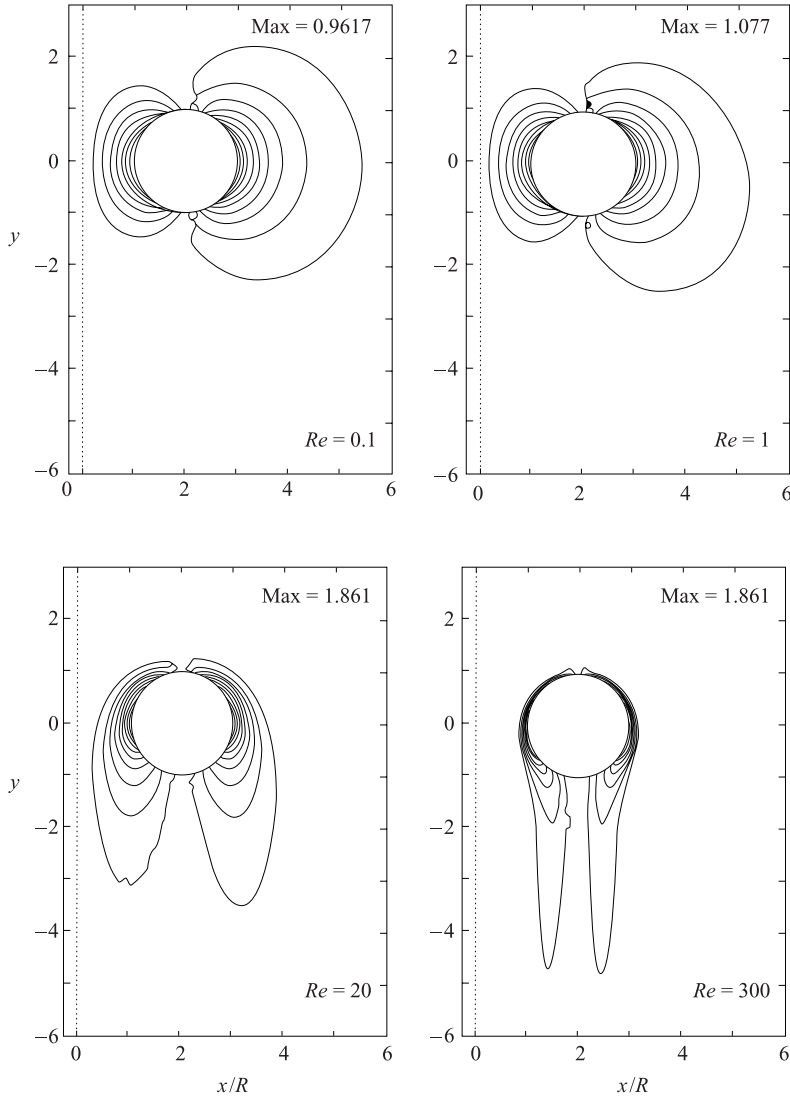
FIGURE 9. Iso-contours of the normalized vorticity $\omega_z = R/U_\infty(\nabla \times V) \cdot e_z$ in the symmetry plane $z = 0$. The difference between two successive iso-contours is $\Delta\omega_z = |\omega_z|_{max}/10$.

The explanation of this evolution may be found in figure 9 where the distribution of the vorticity ω_z in the symmetry plane $z = 0$ is shown for the separation $S = 4$. After it is generated on the bubble surface by the shear-free condition, vorticity diffuses around the bubble and is advected downstream in the wake. At large Reynolds number ($Re = 300$ in figure 9), the distribution of ω_z is almost symmetric with respect to the symmetry plane $x = 0$ (dotted line on figure 9). Hence at leading order the second bubble does not affect the vorticity distribution and the iso-contours would be almost identical to those shown in figure 9 if the bubble were alone (however note that there is a tiny difference in the shape of the iso-contours at about $y = -4.5$). Because of this almost symmetrical vorticity distribution, we may infer that most of the asymmetry of the velocity field observed in figure 8(*b*) at this Reynolds number is
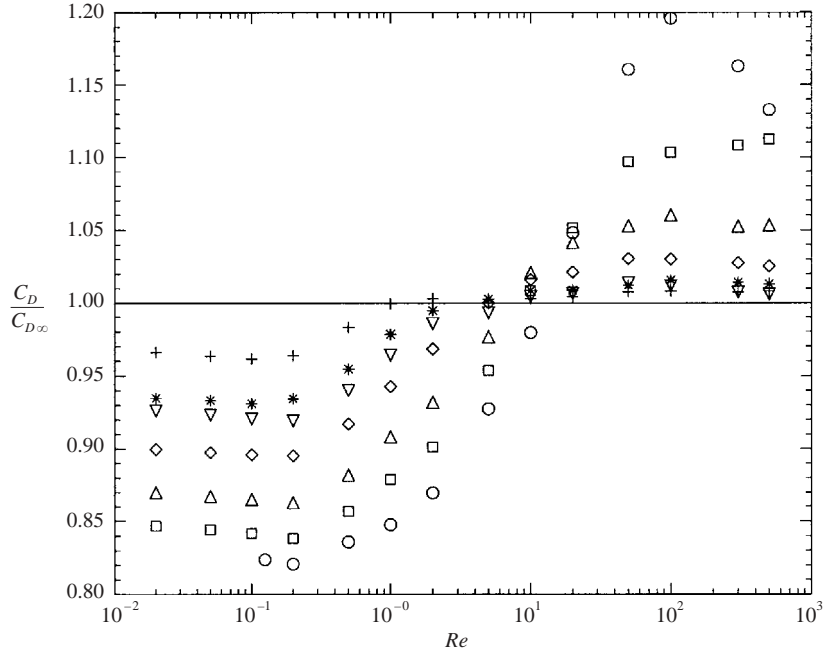
FIGURE 10. Drag ratio $C_D(Re, S)/C_{D\infty}$. $\bigcirc$, $S = 2.25$; $\square$, $S = 2.5$; $\triangle$, $S = 3$; $\diamond$, $S = 4$; $\triangledown$, $S = 5$; $*$, $S = 6$; $+$, $S = 10$.

due to the irrotational mechanism described in §3.4. Therefore the interaction force is certainly negative, as predicted by potential flow theory. When the Reynolds number decreases, the asymmetry between the iso-contours of ω_z becomes more prominent ($Re = 20$). At low Reynolds number ($Re = 1$ and 0.1), the iso-contours located near the symmetry plane $x = 0$ flatten dramatically. It is then clear that the diffusion of ω_z is blocked by the second bubble, making the vorticity distribution strongly asymmetric. In the frame of reference moving with the bubble, the vorticity generated at the surface induces upward velocities which lower the downward irrotational contribution. As the iso-contours of the vorticity are tightened in the gap by the presence of the second bubble, these upward velocities reach their maximum in this region, resulting in a minimum of the overall vertical velocity as we saw in figure 8. Hence the pressure gradient is now directed towards the symmetry plane $x = 0$ and the transverse force is repulsive.

6. Hydrodynamic forces at finite Reynolds number

6.1. *The drag force*

To appreciate the modification of the drag force due to the hydrodynamic interaction, we compare the drag coefficient $C_D(Re, S)$ with the drag coefficient of a single bubble rising at the same Reynolds number, i.e. $C_{D\infty} = C_D(Re, S \to \infty)$. The drag ratio $C_D(Re, S)/C_{D\infty}$ is plotted in figure 10, which clearly shows that the effect of the interaction depends on both separation and Reynolds number. We first note that, while the interaction increases the drag for Reynolds numbers larger than 5 to 10, it decreases it for smaller Reynolds numbers. These trends are in qualitative agreement

with the asymptotic expressions (8) and (12*a*). At large Reynolds number we see that a significant increase (larger than 5%, say) of the drag force due to the interaction occurs only for small separations, typically $S \leqslant 3$. In contrast, the interaction effect extends over larger distances at low Reynolds number; for instance a decrease of the drag by the same amount of 5% is observed for $S \approx 8$. Note that the opposite variations of the drag force observed in the low- and high-Reynolds-number limits imply that for each separation S there is a limit curve $Re_D(S)$ along which both effects cancel exactly, so that $C_D(Re_D, S) = C_{D\infty}(Re_D)$ (this curve appears in figure 17*a* below, where it can be observed that the larger the separation S, the smaller the value of Re_D; for instance we find approximately $Re_D \approx 10$ for $S = 2.5$ and $Re_D \approx 1.5$ for $S = 10$).

In the high-Reynolds-number regime, the drag force on a single spherical bubble, correct to $O(Re^{-3/2})$, was given by Moore (1963) as

$$C_D(Re) = \frac{48}{Re}\left(1 - \frac{2.21}{Re^{1/2}}\right) + O\left(Re^{-5/6}\right). \tag{15}$$

The leading term in (15) is identical to that in (8) in the limit $S \to \infty$. This term corresponds to the drag experienced by a spherical bubble moving in a viscous potential flow with an infinitely thin sheet of vorticity at the bubble surface. The second-order term in (15) is due to finite-Reynolds-number effects. More precisely, it accounts for the presence of a boundary layer of finite thickness and a thin wake behind the bubble. Compared with the 'potential' prediction, these two vortical regions are found to decrease the dissipation in the fluid because vorticity reduces velocity gradients near the bubble surface. The leading-order effect of the interaction on the contribution to the drag force due to the boundary layer and wake may easily be found by the following reasoning. In the irrotational approximation, the flow about the bubble centred at $x = d/2$, $y = z = 0$ is obtained by placing a dipole of strength $-1/2$ at this point, while the symmetry condition on the plane $x = 0$ is satisfied by placing a dipole of similar strength at the image point $x = -d/2$, $y = z = 0$. Expanding the velocity field produced by this image dipole in the vicinity of the original bubble immediately shows that its leading-order term is $-S^{-3}/2\boldsymbol{e}_y$. Hence the bubble feels a vertical velocity equal to $-U_\infty(1 + S^{-3}/2)\boldsymbol{e}_y + o(S^{-3})$, so that the potential and vortical disturbances in the velocity field are multiplied by $1 + S^{-3}/2 + o(S^{-3})$. Now, since the rate of work $\boldsymbol{F}_D \cdot U_\infty \boldsymbol{e}_y$ of the drag force $\boldsymbol{F}_D$ is just balanced by the dissipation in the whole volume of fluid that surrounds the bubble (Batchelor 1967, p. 368), we see that compared to the case of an isolated bubble, this dissipation is multiplied by $1 + S^{-3} + o(S^{-3})$, being a quadratic function of the velocity gradients. Thus we conclude that the leading-order effect of the interaction on the drag force is to multiply Moore's expression (15) by $1 + S^{-3}$ (note that S^{-3} is indeed the leading-order term in the function $g(S)$ given in (8)). Figure 11, for Reynolds numbers larger than 20, compares the difference $C_{Dblw} = 48(1 + g(S))/Re - C_D(Re, S)$ between the 'potential' prediction (8) and the actual drag coefficient $C_D(Re, S)$ with Moore's correction $48 \times 2.21/Re^{3/2}$ multiplied by $1 + S^{-3}$. The agreement is found to be very satisfactory whatever the separation distance as long as the Reynolds number is larger than 30. Note however that, since the contribution of the S^{-3} factor in C_{Dblw} is always less than 10% (with C_{Dblw} itself being less than 20% of $C_D(Re, S)$ for $Re > 50$), its influence is hardly seen in figure 11. Despite this limitation, figure 11 and the theoretical argument given above allow us to write an improved expression for the
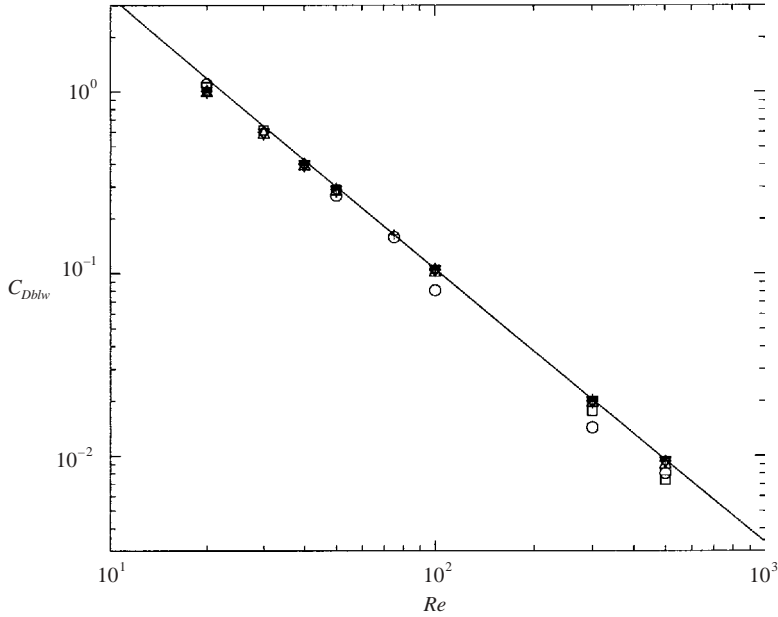
FIGURE 11. Effect of the boundary layer and wake on the drag force at moderate-to-large Reynolds number. $\circ$, $S = 2.25$; $\square$, $S = 2.5$; $\triangle$, $S = 3$; $\diamond$, $S = 4$; $\triangledown$, $S = 5$; $*$, $S = 6$; $+$, $S = 10$; ——, analytical prediction $2.211 \times 48(1 + S^{-3})/Re^{3/2}$.

drag force in the moderate-to-large Reynolds number regime in the form

$$C_D(Re, S) \approx \frac{48}{Re}\left(1 + g(S) - (1 + S^{-3})\frac{2.211}{Re^{1/2}} + O\left(Re^{-5/6}\right)\right), \qquad (16)$$

with $g(S)$ given in (8).

As we saw above, the decrease of the drag force due to the interaction is significant over a wide range of separations at low-to-moderate Reynolds number. Moreover figure 10 shows that this decrease is almost independent of the Reynolds number for $Re < 0.2$. To study the low-Re behaviour of the drag force in more detail, we introduce the function

$$h(Re, S) = C_D(Re, S)/C_{D\infty}(Re),$$

with $C_{D\infty}(Re)$ as defined above. According to the prediction (12a), $h(Re, S)$ should tend towards

$$h_1(Re, S) = \left(1 + Re/8 - e^{-Re\,S/4}/2S\right)/(1 + Re/8)$$

when the conditions $S^{-1} \ll Re \ll 1$ are satisfied. Similarly, according to (14a), it should tend towards

$$h_2(Re, S) = [(1 + (2S)^{-1})(1 + Re/8)]^{-1}$$

when $Re \ll S^{-1} \ll 1$. The numerical values of $h(Re, S)$ are plotted in figure 12 for Reynolds numbers up to 0.2. Values corresponding to $Re = 0.2$ are found to be in excellent agreement with the prediction (12a) whatever S, whereas they are underpredicted by (14a) because the constraint $Re \ll S^{-1}$ is not satisfied. Conversely, for $Re = 0.02$, we see that (12a) underpredicts the effect of the interaction for all S because the constraint $S^{-1} \ll Re$ is never satisfied. At this Reynolds number, (14a) is found to predict accurately $h(Re, S)$ for $S < 4$, approximately.
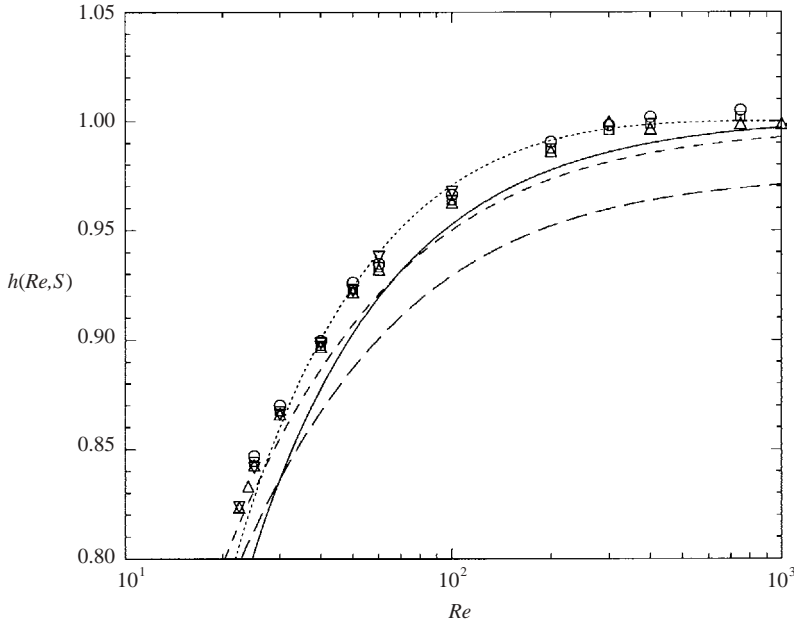
FIGURE 12. Drag ratio $h(Re, S) = C_D(Re, S)/C_{D\infty}(Re)$ at low Reynolds number. $\bigcirc$, $Re = 0.02$; $\square$, $Re = 0.05$; $\triangle$, $Re = 0.1$; $\bigtriangledown$, $Re = 0.2$. ——, $h_1(Re = 0.02, S)$ as predicted by (12a); $\cdots\cdots$, $h_1(Re = 0.2, S)$ as predicted by (12a); - - - -, $h_2(Re = 0.02, S)$ as predicted by (14a); ——, $h_2(Re = 0.2, S)$ as predicted by (14a).

6.2. *The transverse force*

Figure 13 displays the evolution of the lift coefficient C_L in the range $0.02 \leqslant Re \leqslant 500$, $2.25 \leqslant S \leqslant 10$. The most striking feature revealed by this plot is that for any separation distance the sign of the transverse force is reversed when the Reynolds number crosses a certain critical value Re_c. This value depends on S and lies approximately in the range $30 \leqslant Re_c \leqslant 100$ for the range of separations covered here. Conversely, one may define a critical separation $S_c(Re)$ at which the transverse force changes sign. This reversal was to be anticipated given the opposite signs of the lift coefficients predicted by irrotational flow theory (7), and viscous theory ((12b) and (14b)). On figure 13 one also notices that $|C_L|$ reaches significantly larger values for $Re \to 0$ than for $Re \to \infty$. As the Reynolds number increases, numerical results tend asymptotically towards the irrotational prediction (7). For instance, for $S = 3$, the relative difference between the numerical value $C_L(Re, S)$ and the prediction (7) decreases monotonically from 59% at $Re = 50$ to 7.5% at $Re = 500$.

It is of some interest to examine separately the evolution of the contributions due to the normal viscous stress ($C_{L\mu}$) and pressure (C_{Lp}) in the total lift coefficient. These contributions are shown in figure 14 for $S = 3$ (their evolutions are qualitatively similar for other separations). For Reynolds numbers larger than Re_C, the pressure contribution is negative (i.e. attractive) when the viscous contribution is positive but has a negligible magnitude. More precisely, the relative contribution of $C_{L\mu}$ to the total lift coefficient found for $S = 3$ is about 2.4% at $Re = 100$ and decreases to 0.2% at $Re = 500$. At such Reynolds numbers, the effects of the vorticity on the lift force are almost entirely contained in the pressure lift coefficient C_{Lp}, since this contribution differs from the irrotational prediction (7) by about 8% for $Re = 500$ and
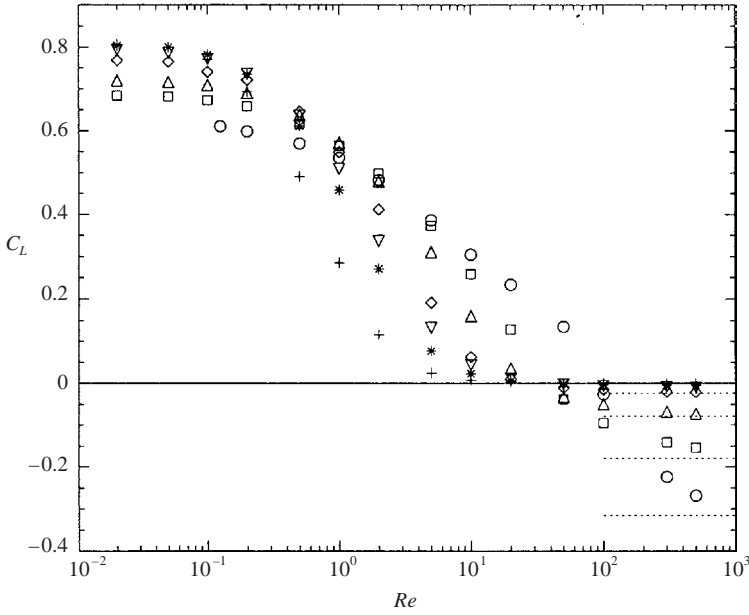
FIGURE 13. Lift coefficient C_L vs. Re for various separations. $\bigcirc$, $S = 2.25$; $\square$, $S = 2.5$; $\triangle$, $S = 3$; $\diamond$, $S = 4$; $\triangledown$, $S = 5$; $*$, $S = 6$; $+$, $S = 10$; $---$, irrotational prediction (7).
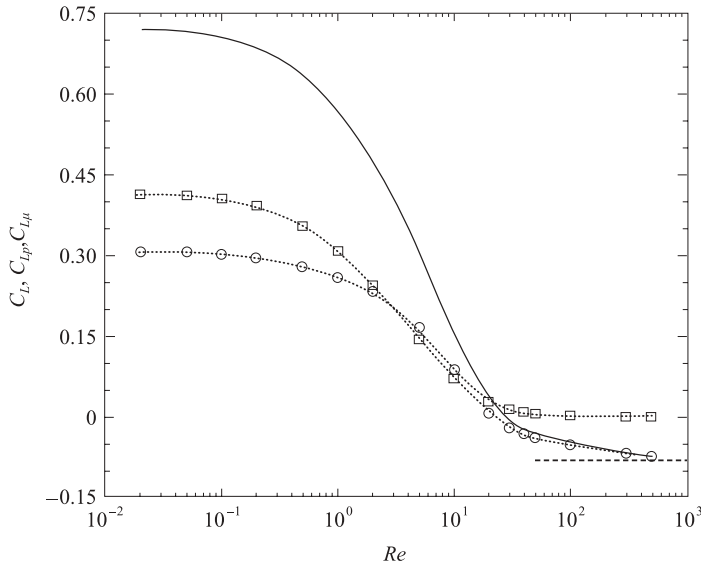

FIGURE 14. Contribution of pressure and normal viscous stress to the total lift force ($S = 3$). $\bigcirc$, C_{Lp}; $\square$, $C_{L\mu}$; ——, $C_L = C_{Lp} + C_{L\mu}$.

this difference increases up to 37% for $Re = 100$. As the Reynolds number decreases in the range $Re < Re_c$, the magnitude of the repulsive contribution $C_{L\mu}$ increases while the pressure contribution C_{Lp} itself becomes repulsive and increases in magnitude. The transverse force is then repulsive. Note that the ratio $C_{L\mu}/C_{Lp}$ tends towards a constant value larger than unity at low Reynolds number.
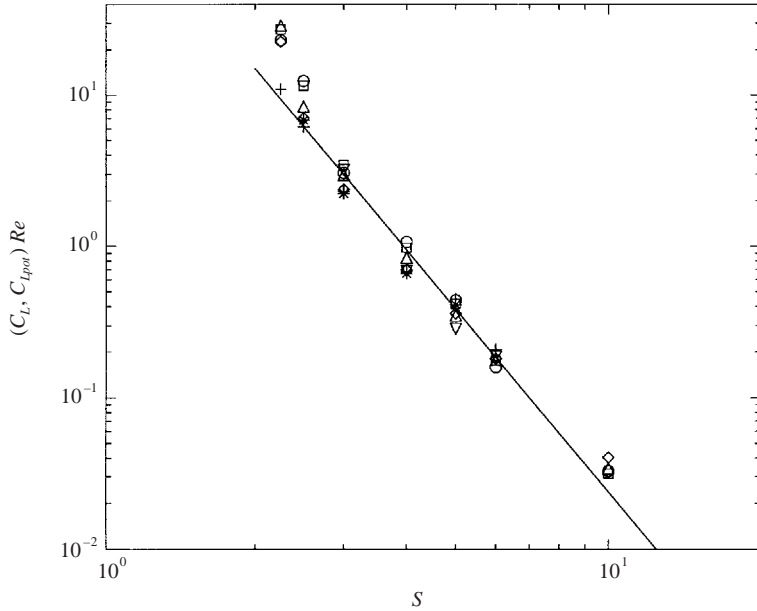
FIGURE 15. Effects of vorticity on the lift force at large Reynolds number. Numerical values of $Re\Delta C_{Lvort}$ for: $\circ$, $Re = 500$; $\square$, $Re = 300$; $\triangle$, $Re = 100$; $\diamond$, $Re = 50$; $\triangledown$, $Re = 40$; $*$, $Re = 30$; $+$, $Re = 20$; ——, $Re\Delta C_{Lvort} = 240S^{-4}$.

To quantify the effects of the vorticity on the transverse force in the high-Reynolds-number regime we may consider the correction $\Delta C_{Lvort} = C_L - C_{Lpot}$ where C_{Lpot} corresponds to the irrotational prediction (7). Let us first discuss the scaling law followed by this correction. As we saw above, the leading-order velocity disturbance produced by the image dipole in the vicinity of the original bubble (i.e. near $x = d/2$, $y = z = 0$) is $-S^{-3}/2e_y$. The next term of this disturbance may be shown to be a strain field $3S^{-4}/2(xe_y + ye_x)$. Hence the first asymmetry with respect to the plane $x = d/2$ in the flow about the bubble occurs at $O(S^{-4})$. This asymmetry is the source of the $O(S^{-4})$ leading-order term in (7). Clearly, it also results in an asymmetry of the vorticity distribution about the bubble. By an order-of-magnitude analysis similar to that of Moore (1963), it may be shown that the leading-order pressure correction associated with this $O(S^{-4})$ vortical velocity is of $O(Re^{-1}S^{-4})$, the next term in the expansion with respect to Re being of $O(Re^{-3/2}S^{-4})$. Hence we expect the leading-order vortical correction ΔC_{Lvort} to the lift coefficient to be proportional to $S^{-4}Re^{-1}$ at large enough Reynolds number. Figure 15 displays the evolution of the quantity $Re\Delta C_{Lvort}$ versus the dimensionless separation S for $20 \leqslant Re \leqslant 500$. In line with the above reasoning, we see that this quantity is almost proportional to S^{-4} for $S \geqslant 3$, the value of the corresponding prefactor being about 240. A more careful examination shows that the values of $Re\Delta C_{Lvort}$ follow a slightly different evolution when the Reynolds number is below 10^2, the slope of the corresponding curve then being somewhat weaker than -4; we shall come back to this point in the next section. Similarly, some deviations are encountered for small separations (say $S < 3$). Given the smallness of the corresponding quantities, it is difficult to determine precisely the variations of $Re\Delta C_{Lvort} - 240S^{-4}$ with S. Nevertheless it seems that this quantity evolves proportionally to S^{-6}. Hence we conclude that for $Re \geqslant 30$ and $S \geqslant 3$, the lift
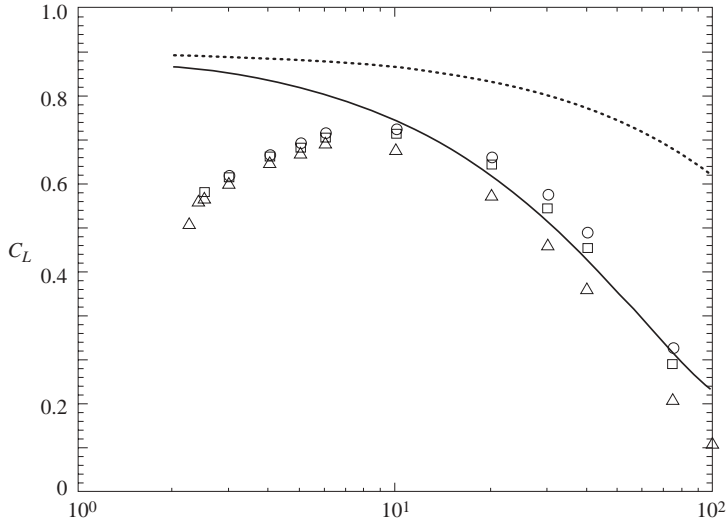
FIGURE 16. Lift coefficient in the low-Reynolds-number regime: ○, $Re = 0.02$; □, $Re = 0.05$; △, $Re = 0.1$; ——, prediction (12b) for $Re = 0.1$; ······, prediction (12b) for $Re = 0.02$.

coefficient may approximately be written as

$$C_L(Re, S) \approx -6S^{-4} \left[\left(1 - \frac{40}{Re} + O\left(Re^{-3/2}\right) \right) + S^{-3} + O(Re^{-1}S^{-2}, S^{-5}) \right]. \quad (17)$$

We now turn to the asymptotic behaviour of the lift coefficient in the low-Reynolds-number regime. Coming back to figure 13, we see that, for $Re < 0.1$, C_L tends towards values that increase slightly with S and are almost independent of the Reynolds number. To study this regime in more detail, we performed numerical simulations at three Reynolds numbers ($Re = 0.1$, 0.05 and 0.02) over a wide range of separations ($2.25 \leqslant S \leqslant 100$). The corresponding values of C_L are plotted in figure 16. The lift coefficient is seen to reach a maximum value of about 0.8 for $S \approx 10$ at each Reynolds number. For smaller separations, C_L decreases slightly and extrapolation of the numerical results towards the limit $S \to 2$ where the two bubbles come in contact suggests a limit value about 0.6. These numerical results may be compared with the analytical predictions (12b) and (14b). For $Re = 0.1$, the constraint $S^{-1} \ll Re$ is approximately satisfied for $S > 20$. Not surprisingly, we observe that for such separations the corresponding numerical values follow the evolution predicted by (12b) (with however a slightly larger slope). In contrast, for $Re = 0.02$, the above constraint is never satisfied for $S < 100$ and (12b) is found to overpredict severely the lift coefficient. It is worth noting that C_L keeps significant values at large separations. For instance one sees that, for $S = 75$, C_L lies in the range 0.21–0.33, depending on Re, and these values correspond to 25% to 40% of the maximum value reached at $S = 10$.

The complementary asymptotic limit $Re \ll S^{-1}$ is approximately reached for $S \leqslant 5$ (resp. $S \leqslant 25$) in the case $Re = 0.1$ (resp. $Re = 0.02$). In this regime, the numerical values of C_L lie between 0.6 and 0.84, depending on the separation. From (14b) we expected these values to be about unity, especially those corresponding to $Re = 0.02$ and $S \geqslant 5$ for which the $O(S^{-2})$ corrections are thought to be small. The reason why the lift coefficient remains 15% to 20% smaller than the theoretical limit derived in the Appendix is unclear and is currently being investigated. It might be due to higher-order corrections neglected in the derivation of (14b), as suggested by the collapse

of the numerical points for $S < 10$. However, we cannot exclude a possible numerical inaccuracy, since the transverse force is very small compared to the drag in this regime. For instance one may see that for $Re = 0.02$ and $S = 5$, the correction experienced by the drag coefficient due to the interaction process, i.e. $\Delta C_D = C_{D\infty}(Re)(1 - h_2(Re, S))$ (see figure 12), is about 75, so that an error of 0.2 on C_L is less than 0.3% of ΔC_D. To ensure that the numerical results are not influenced by artificial confinement effects, we increased the size of the computational domain from $R_\infty/R = 100$ (see §3.2) up to $R_\infty/R = 200$. This did not produce any change in the values of C_L.

6.3. *The equilibrium position*

We saw in figure 13 that the transverse force changes sign for a critical Reynolds number $Re_c(S)$ whatever the separation S. Figure 17(a) shows how the sign of this force evolves in the plane (Re, S); the critical curve corresponding to $C_L = 0$ was obtained by a linear interpolation of the values of C_L found in the computations. Note that the vertical axis of this plot involves the quantity $S - 2$ because this choice is more appropriate to discuss the limit $S \to 2$ where the two bubbles come in contact. According to figure 17(a), the transverse force is always repulsive when the Reynolds number is lower than a critical value $Re_{REP} \approx 28$ corresponding to an equilibrium separation distance $S_c(Re_{REP}) \approx 3$ (note that this is consistent with the low-Reynolds-number prediction (12b) according to which the transverse force is repulsive in this regime, however large S). The critical Reynolds number for which C_L vanishes is found to lie between 30 and 40 for $2.5 \leqslant S \leqslant 8$. It is worth noting that in their recent experimental study of the transverse force acting on a clean spherical bubble rising near a vertical wall, Takemura & Magnaudet (2003) found that this force changes sign when the rise Reynolds number is in the range 30–45, for separations such that $3 \leqslant S \leqslant 8$. Despite the difference between the boundary condition on a rigid wall and that on the symmetry plane considered here, the agreement between the experimental values of the critical Reynolds number and those found in figure 17(a) is noteworthy. The surprising feature of figure 17(a) is that for Reynolds numbers larger than Re_{REP} and separation distances in the range considered here (i.e. $2.25 \leqslant S \leqslant 20$), the critical curve indicates the existence of two equilibrium positions. For instance, the transverse force is found to vanish for both $S_C \approx 2.5$ and ≈ 8 at $Re = 50$. This complex behaviour appears to be related to finite-Re effects not accounted for properly in (17) (see below). To study the stability of the two equilibrium positions, it is convenient to consider the trajectory that a freely moving bubble may follow in the (Re, S)-plane. Since such a bubble moves under the effect of buoyancy, the vertical drag force it experiences is constant all along its path. Equivalently we may say that the quantity $Re^2 C_D(Re, S)$ remains constant, this constant being determined by the value of the Galileo number $Ga = gR^3/\nu^2$, g denoting gravity. The iso-drag curves determined using (16) are plotted in figure 17(b) together with the critical curve $C_L = 0$. From this plot it is clear that only the smallest of the two equilibrium values of S, S_1 say, corresponds to a stable position, because if the separation distance between the two bubbles is increased (resp. decreased) slightly above (resp. below) S_1, the transverse force becomes attractive (resp. repulsive), leading to a decrease of the difference $|S - S_1|$. In contrast, any deviation of S from the largest equilibrium value S_2 tends to increase the difference $|S - S_2|$.

As our computations cover a limited range of separations, we cannot directly determine the asymptotic branches of the critical curve $Re_c(S)$ in the limit of both large ($S \to \infty$) and small ($S \to 2$) separations. However, we may notice that for $S < 3$ the computational results show that Re_c increases when the separation decreases.
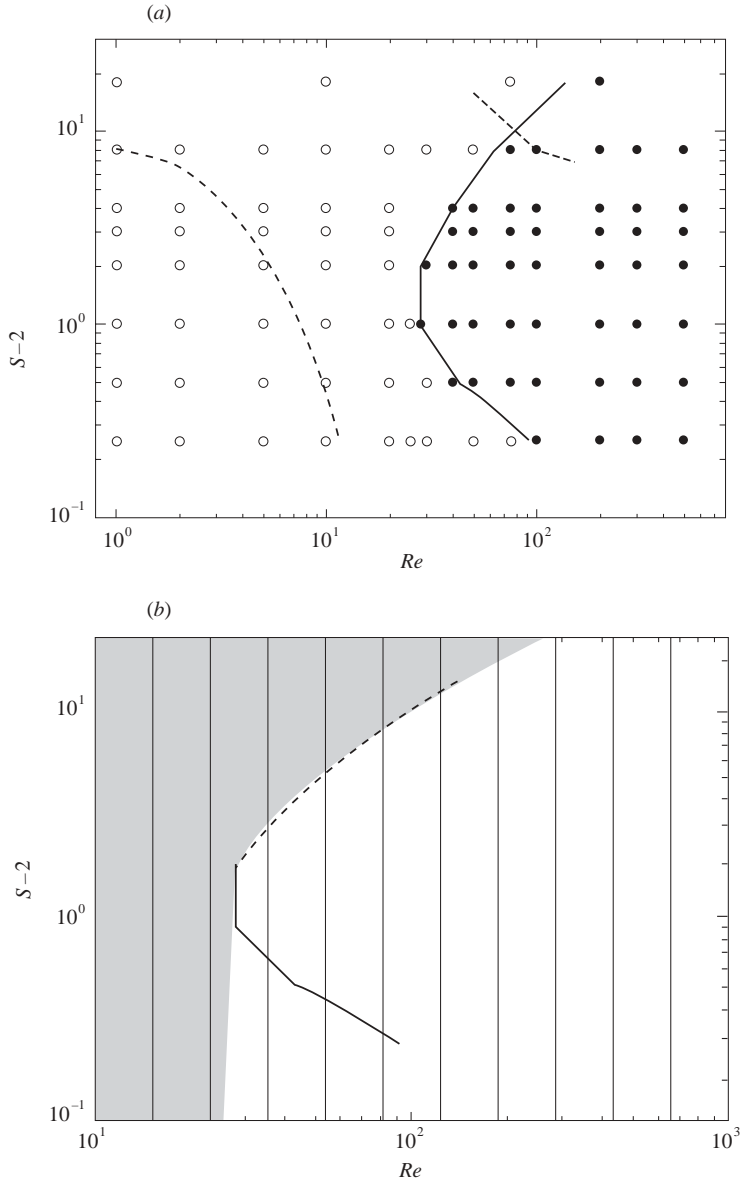
(*a*)

(*b*)

FIGURE 17. Sign of the interaction force in the (Re, S) plane. (*a*) ●, Bubbles are attracted towards each other; ○, bubbles are repelled from each other; —— critical curve corresponding to $C_L = 0$; $----$, limit curve corresponding to $C_D(Re, S) = C_{D\infty}(Re)$; $\cdots\cdots$, critical curve corresponding to $C_L = 0$ for two rigid spheres (Kim *et al.* 1993). (*b*) ——, Iso-drag curves; ——, $S = S_1(Re)$; $-----$, $S = S_2(Re)$. The grey area corresponds to the sub-region of initial separations S_i for which the bubbles subsequently separate up to infinity, while the white area is the basin of attraction of the stable equilibrium position $S = S_1(Re)$.

More precisely, they indicate that the slope of the curve $S_c(Re)$ is about -2 (resp. -1) for $2.5 \leqslant S \leqslant 3$ (resp. $2.25 \leqslant S \leqslant 2.5$). While we cannot settle the matter definitely because lubrication effects certainly appear when $S \rightarrow 2$, these results suggest that the critical Reynolds number Re_c tends to infinity when the two bubbles come in contact.

It is even more difficult to determine how Re_c evolves with S in the opposite limit $S \to \infty$ because the interaction force then tends to zero. We saw in §3.4 that for large Reynolds numbers the accuracy of our computations can be considered sufficient only up to separations $S \approx 20$, which prevents us from drawing a clear conclusion by running computations for larger values of S. Examining figure 17(*a*) for large S, the only obvious feature is that for a given separation the transverse force becomes attractive for high enough Re. However, a better understanding of the increase of Re_c with S in the limit $S \to \infty$ is provided by (12*b*) and (17). While (17) shows that C_L decays as S^{-4} for $S \to \infty$ at high enough Reynolds number, (12*b*) indicates that in the low-Re regime and for a given Re, the transverse (repulsive) force decays as S^{-2} at large S. Hence one may suspect that for moderate Reynolds number, i.e. for Re typically in the range 10–10^2, finite-Re effects at large S have a repulsive contribution proportional to S^{-m} with $2 < m < 4$, the value of m being Re-dependent and tending towards $m = 4$ at large Re, to yield the contribution $240\,S^{-4}Re^{-1}$ found in figure 15. The existence of this repulsive S^{-m} contribution explains why, in the range of Re_c corresponding to the range of S covered by our computations, the critical Reynolds number is found to increase with S at large separations. However, if S becomes very large, this tendency will make Re_c increase sufficiently for (17) to become applicable. Hence we guess that for very large separations, Re_c should be a constant, the value of which is determined by the vanishing of the whole S^{-4} term of (17). Note that considering only the leading-order vortical correction in (17) yields $Re_c \approx 40$ in the limit $S \to \infty$, which clearly underpredicts Re_c. This suggests that the next $O(Re^{-3/2}S^{-4})$ term has a substantial prefactor that makes it contribute significantly to the value of $Re_c(S \to \infty)$.

Collecting all the above information, the following picture emerges. If two clean spherical bubbles initially separated by a dimensionless distance S_i and having a sufficiently large Galileo number (so that their rise Reynolds number exceeds Re_{REP}) are released with their line of centres horizontal, then depending on S_i being larger or smaller than $S_2(Ga)$, they will either move apart from each other up to infinity or will move towards or apart from each other until they reach the stable equilibrium position $S = S_1(Ga)$. In contrast, if the Galileo number is too small for Re to exceed Re_{REP}, they will be repelled from each other up to infinity whatever S_i. The subdomain corresponding to values of S_i for which the two bubbles move apart from each other to infinity is coloured grey in figure 17(*b*). In figure 17(*a*) we also report the critical curve $C_L = 0$ that can be determined from the numerical results of Kim *et al.* (1993) for two rigid spheres settling side by side. These authors explored a more narrow range of Re and S than we did but their results clearly show that the transverse force becomes attractive when the Reynolds number exceeds some critical, S-dependent, value. The existence of such a critical Reynolds number for both bubbles and rigid spheres strongly suggests that the process leading to the force reversal is qualitatively similar in both cases. As we saw in §6.2, the sign of the transverse force acting on a pair of bubbles is governed by the competition between the irrotational mechanism associated with the asymmetrical deflection of the fluid between and around the bubbles and the wake/boundary layer phenomena resulting from the asymmetric generation, diffusion and transport of vorticity around them. This picture is general and applies to rigid particles as well as to bubbles; only the amount of vorticity generated on the particle surface differs between the two types of particles. As more vorticity is generated on a rigid sphere than on a spherical bubble for a given Reynolds number, the subdomain of the (Re, S)-plane where the transverse force is repulsive is larger in the former case.

7. Summary and conclusions

In this paper we have studied numerically the interaction between two clean spherical bubbles rising side by side in a viscous fluid at rest at infinity. We explored a wide range of Reynolds number in order to describe situations dominated by viscous effects as well as nearly inviscid cases. As the transverse force is generally small compared to the drag component, a careful preliminary check of the numerical accuracy was necessary. Analytical results available in the potential flow limit were extensively used for this purpose and an excellent agreement with theoretical predictions was found for the stationary drag and lift forces as well as for the added-mass force, up to dimensionless separations at which the effect under consideration becomes very small.

As is well known, the acceleration of the flow in the gap separating the two bubbles yields an attractive interaction force in the potential flow limit. In contrast, our analytical extension of Vasseur & Cox's (1977) result to a pair of shear-free bubbles shows that this force is repulsive in the low-Reynolds-number limit because the vorticity produced at the bubble surfaces induces upward velocities, thus resulting in vertical velocities in the gap smaller than the rising speed. The computational results confirmed the role played by the vorticity produced at the bubble surface, even at moderate-to-high Reynolds number. In particular they showed that bubbles with a Reynolds number lower than a critical value Re_{REP} of the order of 30 are repelled however large their initial separation S_i, while at higher Reynolds number bubbles are repelled from each other up to infinity only if they are released with a separation S_i larger than a critical value $S_2(Re)$. In the opposite case where S_i is smaller than $S_2(Re)$, bubbles tend to reach an equilibrium configuration corresponding to a separation $S = S_1(Re)$ with $S_1(Re) < S_2(Re)$, $S_1(Re)$ being a decreasing function of the Reynolds number, which is about 3 (corresponding to a gap thickness about one bubble radius) for $Re = 30$. We note that this behaviour is not specific to bubbles, having also been observed at sufficiently large values of Re and S for rigid spheres by Kim *et al.* (1993).

Overall, the present results indicate that interaction effects arising between two clean spherical bubbles rising side by side at Reynolds numbers less than say 250 (i.e. the upper limit for which deformation effects may be reasonably neglected in pure water) are not satisfactorily described in the classical framework of potential flow theory since this theory predicts that the interaction force is attractive whatever S. In particular these results question the applicability in the above range of Re of the 'direct' potential computations performed by Sangani & Didwania (1993) and Smereka (1993) for a cloud of spherical bubbles rising under the effect of buoyancy in a periodic box. In contrast with the systematic formation of stable horizontal clusters observed in those simulations, the existence of a repulsive interaction force for small-to-moderate rise Reynolds numbers and of an equilibrium (admittedly small) separation distance for higher Reynolds numbers favours a more homogeneous spatial distribution of the bubbles. We indeed found that the interaction force is positive for Re larger than 50–100 (depending on S), so that horizontal clustering is likely to occur in the range $100 \leqslant Re \leqslant 250$. However, the actual attractive force is significantly smaller than predicted by irrotational theory, indicating that the clustering process requires a longer time than found in the aforementioned irrotational computations.

For Reynolds numbers higher than those covered by the present study, deformation can no longer be neglected and the oblateness of the bubbles has to be taken into account. Associated with this increased curvature of the bubbles near their equator is an increased generation of vorticity on their surface which yields an instability of

the wake for bubbles with an aspect ratio larger than about 2, corresponding to rise Reynolds numbers larger than 600, approximately. It was recently shown (Mougin & Magnaudet 2002b) that this wake instability is the cause of the zigzagging/ spiralling motion of clean millimetric bubbles rising in low-viscosity liquids. As these additional horizontal motions significantly increase the agitation in the surrounding liquid, several authors are currently exploring the possibility that they may explain why the horizontal clustering predicted by the irrotational flow model is not detected experimentally. This idea follows from the statistical arguments presented by Yurkovetsky & Brady (1995) and Spelt & Sangani (1998) who showed that the larger the r.m.s. velocity fluctuations of the liquid relative to the rise velocity, the smaller the tendency for horizontal clusters to form. If this effect of horizontal motions is confirmed, it would mean that vorticity effects play a crucial role in the dynamics of bubbly suspensions over the whole range of Re corresponding to spheroidal bubbles, since on the one hand they produce a repulsive force in the low-to-moderate Re regime, and on the other hand are responsible for the high-Re wake instability by which zigzagging/spiralling motions preventing clustering are generated.

Coming back to spherical bubbles, we note that the fact that finite-Re effects favour a more homogeneous distribution that predicted by irrotational theory is not limited to the side-by-side configuration. Indeed the same was observed in the computations of Yuan & Prosperetti (1994) for two bubbles rising in line, as these authors found that wake effects result in the existence of an equilibrium separation distance ranging from $S \approx 3$ for $Re = 50$ to $S \approx 6$ for $Re = 200$. Expressions (16) and (17) may be seen as the starting point of a realistic model of steady and quasi-steady hydrodynamic forces experienced by interacting bubbles moving at moderate-to-high Reynolds number, as they take into account inviscid interaction effects, high-Reynolds-number corrections due to vorticity in the boundary layer and wake of each bubble, and the leading-order interaction between both effects. Of course it would be helpful to derive analytically the numerical prefactor of the $S^{-4}Re^{-1}$ term in (17) by solving the boundary layer equations in the asymmetric situation considered here. As the present investigation only considered the particular case of two bubbles rising at a right angle to their line of centres, it would also be of interest to generalize the present approach by examining how the leading-order vortical corrections derived here change with the angle θ between the line of centres and the direction of rise (in the potential flow limit, this general situation was considered by Kok (1993a) who obtained closed-form expressions for the changes in the drag and lift forces due to interaction effects). Given the results of Yuan & Prosperetti (1994) for the in-line configuration ($\theta = \pi$) and the present ones for the side-by-side configuration ($\theta = \pi/2$), we guess that an equibrium surface $S_c(Re, \theta)$ exists whatever θ. We believe that exploring how S_c evolves with θ and developing general approximate expressions for the hydrodynamic forces acting on a pair of bubbles in the moderate-to-high Reynolds number regime would open new possibilities for obtaining realistic, relatively low-cost, descriptions of the concentrated bubbly suspensions involved in many applications.

Appendix. The drag and lift coefficients in the limit $Re \ll S^{-1} \ll 1$

In this appendix we derive the low-Reynolds-number expression for the drag and lift forces acting on a pair of bubbles filled with a gas of negligible viscosity in the asymptotic limit where the second bubble lies in the inner (Stokes) region of the disturbance produced by the first one, the separation between the two bubbles being large compared to their radius. Distances are made dimensionless using the bubble

radius R, while velocities are normalized by the rise velocity U_∞. We choose a system of axes translating with the bubbles, with the origin $x_1 = x_2 = x_3 = 0$ at the centre of one of them (say B 1), x_1 being directed away from the second bubble (say B 2) and x_2 directed vertically upwards; the corresponding unit vectors are e_1, e_2 and e_3, respectively. Note that with these choices B 2 is centred at $x_1 = -S$, $x_2 = x_3 = 0$ and the upstream velocity is $-e_2$. At leading order, the velocity field $U^{(0)}$ about the two bubbles is obtained by inserting two Stokeslets of strength $1/2$ at the bubble centres, namely

$$U^{(0)} = -e_2 + \frac{1}{2}\left(\frac{e_2}{r} + \frac{x_2 x}{r^3}\right) + \frac{1}{2}\left(\frac{e_2}{r^*} + \frac{x_2(x + Se_1)}{r^{*3}}\right), \tag{A 1}$$

where $x = x_1 e_1 + x_2 e_2 + x_3 e_3$, $r = (x_1^2 + x_2^2 + x_3^2)^{1/2}$ and $r^* = ((x_1 + S)^2 + x_2^2 + x_3^2)^{1/2}$. The velocity field $U^{(0)}$ satisfies Stokes equations everywhere in the liquid, is symmetric with respect to the plane $x_1 = -S/2$ and tends towards the undisturbed velocity $-e_2$ at infinity. Combined with this undisturbed velocity, each of the two Stokeslets would also satisfy the impermeability and shear-free conditions on the corresponding bubble if this bubble were alone. However the resulting velocity $U^{(0)}$ does not satisfy these two conditions because each Stokeslet creates a disturbance near the other bubble. Assuming that $S/2 \gg 1$, we can expand the velocity field due to the Stokeslet corresponding to B2, say U^*, in the vicinity of B 1. This yields

$$U^*(r/S \ll 1) = \tfrac{1}{2}S^{-1}e_2 - S^{-2}(x_1 e_2 - x_2 e_1) + O(S^{-3}). \tag{A 2}$$

Thus we see that the boundary conditions are satisfied on B 1 (resp. B 2) up to $O(S^{-2})$ provided we introduce a new Stokeslet of strength $-\tfrac{1}{4}S^{-1}$ at the origin (resp. at $x_1 = -S$, $x_2 = x_3 = 0$). In other words, the velocity correction $U^{(c)}$ to be added to $U^{(0)}$ at $O(S^{-1})$ to satisfy the boundary conditions on the two bubbles is

$$U^{(c)} = -\frac{S^{-1}}{4}\left[\left(\frac{e_2}{r} + \frac{x_2 x}{r^3}\right) + \left(\frac{e_2}{r^*} + \frac{x_2(x + Se_1)}{r^{*3}}\right)\right] + O(S^{-2}). \tag{A 3}$$

We note that the $O(S^{-2})$ term in (A 2) is a solid-body rotation which does not induce any additional stress, i.e. no stresslet is required to satisfy the zero-shear-stress condition at $O(S^{-2})$, unlike what happens for a bubble rising near a rigid wall (see Magnaudet *et al.* 2003). Similarly, it can be proved that higher-order singularities associated with terms of $O(S^{-n})$ $(n \geqslant 3)$ in the expansion of U^* near B 1 do not involve any Stokeslet, being only Stokes quadrupoles, octupoles, etc. However, the reflection of these higher-order singularities on B 2 necessarily induces constant velocity corrections near B 1, and hence new Stokeslets at $O(S^{-2n})$. On the other hand, repeating the above reasoning shows that the Stokeslet of strength $-\tfrac{1}{4}S^{-1}$ at B 2 requires a new Stokeslet of strength $\tfrac{1}{2}(-\tfrac{1}{2}S^{-1})^2$ at B 1, etc. Neglecting Stokeslets of $O(S^{-2n})$ with $n \geqslant 3$ resulting from the reflections of higher-order singularities, it turns out that the total strength of the Stokeslets produced by the successive reflections of the initial Stokeslet of strength $1/2$ is

$$\tfrac{1}{2}\left[1 - \tfrac{1}{2}S^{-1} + \left(\tfrac{1}{2}S^{-1}\right)^2 - \left(\tfrac{1}{2}S^{-1}\right)^3 + ...\right] = \frac{1}{2 + S^{-1}}. \tag{A 4}$$

As we know from the Hadamard–Rybczyinski formula that a Stokeslet of strength $1/2$ corresponding to an isolated bubble yields a drag coefficient $C_D = 16/Re$, we conclude that the drag coefficient of a pair of bubbles moving perpendicular to their

line of centres is, in the present asymptotic limit,

$$C_D(S) = \frac{16}{Re} \left[\frac{1}{1 + (2S)^{-1}} + O(S^{-6}) \right]. \tag{A 5}$$

This result shows that the low-Reynolds-number interaction process decreases the drag force, compared to that experienced by an isolated bubble. In particular, in the limit where the two bubbles come in contact ($S = 2$), (14) suggests that the drag force is approximately 4/5 of that acting on a single bubble.

To obtain the lift force in the same asymptotic limit, we first consider the auxiliary Stokes problem corresponding to the flow generated by two bubbles centred at $x_1 = x_2 = x_3 = 0$ and $x_1 = -S, x_2 = x_3 = 0$, respectively, and moving with opposite velocities of unit magnitude along their line of centres. The leading-order velocity field $\boldsymbol{u}^{(0)}$ corresponding to this situation is clearly

$$\boldsymbol{u}^{(0)} = -\boldsymbol{e}_1 + \frac{1}{2}\left(\frac{\boldsymbol{e}_1}{r} + \frac{x_1\boldsymbol{x}}{r^3}\right) - \frac{1}{2}\left(\frac{\boldsymbol{e}_1}{r^*} + \frac{x_1(\boldsymbol{x} + S\boldsymbol{e}_1)}{r^{*3}}\right). \tag{A 6}$$

As required by the symmetry of the problem, the tangential velocity is zero on the plane $x_1 = -S/2$, while the normal velocity is -1, owing to the unit x_1-translation of the coordinate system. Expanding the velocity field due to the second Stokeslet in (A 6), say $\boldsymbol{u}^*$, in the vicinity of the first bubble, we obtain

$$\boldsymbol{u}^*(r/S \ll 1) = -S^{-1}\boldsymbol{e}_1 + O(S^{-2}). \tag{A 7}$$

Thus, up to terms of $O(S^{-2})$, the velocity correction $\boldsymbol{u}^{(c)}$ to be added to $\boldsymbol{u}^{(0)}$ in order to satisfy the impermeability and shear-free conditions on the two bubbles is merely

$$\boldsymbol{u}^{(c)} = \frac{S^{-1}}{2}\left[\left(\frac{\boldsymbol{e}_1}{r} + \frac{x_1\boldsymbol{x}}{r^3}\right) - \left(\frac{\boldsymbol{e}_1}{r^*} + \frac{x_1(\boldsymbol{x} + S\boldsymbol{e}_1)}{r^{*3}}\right)\right] + O(S^{-2}). \tag{A 8}$$

Let us now consider the velocity fields $\boldsymbol{U} = \boldsymbol{U}^{(0)} + \boldsymbol{U}^{(c)}$ (given by (A 1) and (A 3)) and $\boldsymbol{u} = \boldsymbol{u}^{(0)} + \boldsymbol{u}^{(c)}$ (given by (A 6) and (A 8)). Up to corrections of $O(S^{-2})$, these are the solutions of the Stokes equations for the 'direct' problem of two bubbles rising side by side and for the 'auxiliary' problem of two bubbles moving with opposite velocities along their line of centres, respectively. Then, provided the distance between each bubble and the symmetry plane $x_1 = -S/2$ is smaller than the Oseen radius Re^{-1}, i.e. the condition $Re \ll S^{-1}$ is satisfied, it is known since the work of Cox & Brenner (1968) that $O(Re)$ inertial effects can be evaluated using the above Stokes solutions only, without having to consider the contributions of the corresponding outer expansions. Then, using the reciprocal theorem (see e.g. Magnaudet *et al.* 2003 and references therein) the lift coefficient correct up to corrections of $O(S^{-2})$ is given by

$$C_L = -\frac{2}{\pi} \int_{V_F} (\boldsymbol{u} + \boldsymbol{e}_1) \cdot (\boldsymbol{U} \cdot \nabla)\boldsymbol{U} \, dV, \tag{A 9}$$

where V_F denotes the entire volume of liquid corresponding to the half-space $x_1 > -S/2$. To evaluate the volume integral in (A 9) it is convenient to re-express $\boldsymbol{u}$ and $\boldsymbol{U}$ using the outer variables $\overline{x}_i = 2S^{-1}x_i (i = 1, 3), \overline{r} = 2S^{-1}r$ and $\overline{\boldsymbol{x}} = \overline{x}_1\boldsymbol{e}_1 + \overline{x}_2\boldsymbol{e}_2 + \overline{x}_3\boldsymbol{e}_3$. Then, taking into account the transformations $\nabla \equiv 2S^{-1}\overline{\nabla}$ and $dV \equiv \frac{1}{8}S^3 \, d\overline{V}$, (A 9)

becomes

$$C_L = \frac{1}{2\pi}\left(1 + \frac{1}{2}S^{-1}\right)\underbrace{\int_{\overline{V_F}} \bar{\boldsymbol{u}}_{Sto}\cdot(\boldsymbol{e}_2\cdot\bar{\boldsymbol{\nabla}})\bar{\boldsymbol{U}}_{Sto}\,\mathrm{d}\bar{V}}_{I} - \frac{S^{-1}}{2\pi}\underbrace{\int_{\overline{V_F}} \bar{\boldsymbol{u}}_{Sto}\cdot(\bar{\boldsymbol{U}}_{Sto}\cdot\bar{\boldsymbol{\nabla}})\bar{\boldsymbol{U}}_{Sto}\,d\bar{V}}_{J} + O(S^{-2}),$$

(A 10)

where $\overline{V_F}$ denotes the entire half-space $\overline{x_1} > -1$ and $\bar{\boldsymbol{U}}_{Sto}$ and $\bar{\boldsymbol{u}}_{Sto}$ are given by

$$\bar{\boldsymbol{U}}_{Sto} = \left(\frac{\boldsymbol{e}_2}{\bar{r}} + \frac{\overline{x_2\boldsymbol{x}}}{\bar{r}^3}\right) + \left(\frac{\boldsymbol{e}_2}{\bar{\tau}} + \frac{\overline{x_2(\bar{\boldsymbol{x}} + 2\boldsymbol{e}_1)}}{\bar{\tau}^3}\right),$$

$$\bar{\boldsymbol{u}}_{Sto} = \left(\frac{\boldsymbol{e}_1}{\bar{r}} + \frac{\overline{x_1\boldsymbol{x}}}{\bar{r}^3}\right) - \left(\frac{\boldsymbol{e}_1}{\bar{\tau}} + \frac{\overline{x_1(\bar{\boldsymbol{x}} + 2\boldsymbol{e}_1)}}{\bar{\tau}^3}\right),$$

with $\bar{\tau} = (\overline{x_2}^2 + \overline{x_3}^2 + (\overline{x_1} + 2)^2)^{1/2}$.

The two integrals in (A 10) may first be reduced to double integrals by setting $\overline{x_2} = \bar{\rho}\cos\psi$, $\overline{x_3} = \bar{\rho}\sin\psi$ and integrating analytically with respect to ψ, which in both cases yields a factor of π. The resulting double integrals can be evaluated using contour integration. To save time we chose to evaluate them numerically with an accuracy of three digits. The resulting values are $I = 2\pi$, $J = \pi$, from which we obtain

$$C_L = 1 + O(S^{-2}).$$

(A 11)

REFERENCES

BATCHELOR, G. K. 1967 *An Introduction to Fluid Dynamics*. Cambridge University Press.

BATCHELOR, G. K. 1971 The stress generated in a non-dilute suspension of elongated particles by pure straining motion. *J. Fluid Mech.* **46**, 813–829.

BATCHELOR, G. K. 1972 Sedimentation in a dilute dispersion of spheres. *J. Fluid Mech.* **52**, 245–268.

BATCHELOR, G. K. & GREEN, J. T. 1972a The hydrodynamic interaction of two small freely-moving spheres in a linear flow field. *J. Fluid Mech.* **56**, 375–400.

BATCHELOR, G. K. & GREEN, J. T. 1972b The determination of the bulk stress in a suspension of spherical particles to order c^2. *J. Fluid Mech.* **56**, 401–427.

BIESHEUVEL, A. & VAN WIJNGAARDEN, L. 1982 The motion of pair of gas bubbles in a perfect liquid. *J. Engng Math.* **16**, 349–365.

BRADY, J. F. & BOSSIS, G. 1988 Stokesian Dynamics. *Annu. Rev. Fluid Mech.* **20**, 111–157.

BUNNER, B. & TRYGGVASON, G. 2002 Dynamics of homogeneous bubbly flows. Part 1. Rise velocity and microstructure of the bubbles. *J. Fluid Mech.* **466**, 17–52.

CALMET, I & MAGNAUDET J. 1997 Large-eddy simulation of high-Schmidt number mass transfer in a turbulent channel flow. *Phys. Fluids* **9**, 1–18.

CHIANG, C. H. & SIRIGNANO, W. A. 1992 Interacting, convecting, vaporizing fuel droplets with variable properties. *Intl J. Heat Mass Transfer* **36**, 875–886.

CLIFT, R., GRACE, J. R. & WEBER, M. E. 1978 *Bubbles, Drops and Particles*. Academic.

COX, R. G. & BRENNER, H. 1968 The lateral migration of solid particles in Poiseuille flow: 1. Theory. *Chem. Engng Sci.* **23**, 147–173.

DUINEVELD, P. C. 1994 Bouncing and coalescence of two bubbles in water. PhD Dissertation, Twente University, The Netherlands.

DURFOLSKY, L., BRADY, J. F. & BOSSIS, G. 1987 Dynamic simulation of hydrodynamically interacting particles. *J. Fluid Mech.* **180**, 21–49.

ESMAEELI, A. & TRYGGVASON, G. 1998 Direct numerical simulations of bubbly flows. Part 1. Low Reynolds number arrays. *J. Fluid Mech.* **377**, 313–345.

ESMAEELI, A. & TRYGGVASON, G. 1999 Direct numerical simulations of bubbly flows. Part 2. Moderate Reynolds number arrays. *J. Fluid Mech.* **385**, 325–358.

HAPPEL, J. & BRENNER, H. 1973 *Low Reynolds Number Hydrodynamics*. Noordhoff.

HARPER, J. F. 1970 On bubbles rising in line at large Reynolds numbers. *J. Fluid Mech.* **41**, 751–758.

HARPER, J. F. 1997 Bubbles rising in line: why is the first approximation so bad? *J. Fluid Mech.* **351**, 289–300.

HINCH, E. J. 1977 An averaged-equation approach to particle interactions in a fluid suspension. *J. Fluid Mech.* **83**, 695–720.

JEFFREY, D. J. 1973 Conduction through a random suspension of spheres. *Proc. R. Soc. Lond.* A **335**, 355–367.

KATZ, C. J. & MENEVEAU 1996 Wake-induced relative motion of bubbles rising in line. *Intl J. Multiphase Flow* **22**, 239–258.

KIM, I., ELGHOBASHI, S. & SIRIGNANO, W. A. 1993 Three-dimensional flow over two spheres placed side by side. *J. Fluid Mech.* **246**, 465–488.

KOK, J. B. W. 1993a Dynamics of a pair of gas bubbles moving through liquid. Part I. Theory. *Eur. J. Mech. B/Fluids* **12**, 515–540.

KOK, J. B. W. 1993b Dynamics of a pair of gas bubbles moving through liquid. Part II. Experiment. *Eur. J. Mech. B/Fluids* **12**, 541–560.

KUMARAN, V. & KOCH, D. L. 1993 The effect of hydrodynamic interactions on the average properties of a bidisperse suspension of high Reynolds number, low Weber number bubbles. *Phys. Fluids* A **5**, 1123–1134.

LEGENDRE, D. & MAGNAUDET, J. 1998 The lift force on a spherical bubble in a viscous linear shear flow. *J. Fluid Mech.* **368**, 81–126.

LEVICH, V. G. 1962 *Physicochemical Hydrodynamics*. Prentice Hall.

MAGNAUDET, J. & EAMES, I. 2000 The motion of high-Reynolds-number bubbles in inhomogeneous flows. *Annu. Rev. Fluid Mech.* **32**, 659–708.

MAGNAUDET, J., RIVERO, M. & FABRE, J. 1995 Accelerated flows past a rigid sphere or a spherical bubble. Part 1. Steady straining flow. *J. Fluid Mech.* **284**, 97–135.

MAGNAUDET, J., TAKAGI, S. & LEGENDRE, D. 2003 Drag, deformation and lateral migration of a buoyant drop moving near a vertical wall. *J. Fluid Mech.* **476**, 115–157.

MEI, R., KLAUSNER, J. F. & LAWRENCE, C. J. 1994 A note on the history force on a spherical bubble at finite Reynolds number. *Phys. Fluids* **6**, 418–420.

MILNE-THOMSON, L. M. 1968 *Theoretical Hydrodynamics*. McMillan.

MILOH, T. 1977 Hydrodynamics of deformable contiguous spherical shapes in an incompressible inviscid fluid. *J. Engng Maths.* **11**, 349–372.

MOORE, D. W. 1963 The boundary layer on a spherical gas bubble. *J. Fluid Mech.* **16**, 161–176.

MOUGIN, G. & MAGNAUDET, J. 2002a The generalized Kirchhoff equations and their application to the interaction of a rigid body with an arbitrary time-dependent viscous flow. *Intl J. Multiphase Flow* **28**, 1837–1851.

MOUGIN, G. & MAGNAUDET, J. 2002b Path instability of a rising bubble. *Phys. Rev. Lett.* **88**, 014502.

OSEEN, C. W. 1927 *Hydrodynamik*. Leipzig; Akademische Verlag.

PATNAIK, G. 1986 A numerical solution of droplet vaporization with convection. PhD Dissertation, Carnegie-Mellon University.

RAJU, M. S. & SIRIGNANO, W. A. 1990 Interaction between two vaporizing droplets in an intermediate-Reynolds-number flow. *Phys. Fluids* A **2**, 1780–1796.

RIVERO, M., MAGNAUDET, J. & FABRE, J. 1991 Quelques résultats nouveaux concernant les forces exercées sur une inclusion sphérique par un écoulement accéléré. *C. R. Acad. Sci. Paris Série II* **312**, 1499–1506.

SANGANI, A. S. & DIDWANIA, A. K. 1993 Dynamic simulations of flows of bubby liquids at large Reynolds numbers. *J. Fluid Mech.* **250**, 307–437.

SMEREKA, P. 1993 On the motion of bubbles in a periodic box. *J. Fluid Mech.* **254**, 79–112.

SPELT, P. D. M. & SANGANI, A. 1998 Properties and averaged equations for flows of bubbly liquids. *Appl. Sci. Res.* **58**, 337–386.

TAKEMURA, F. & MAGNAUDET, J. 2003 The transverse force on a clean or contaminated bubble rising near a vertical wall at moderate Reynolds number. *J. Fluid Mech.* **495**, 235–253.

TAL, T. R., LEE, D. N. & SIRIGNANO, W. A. 1984 Heat and momentum transfer around a pair of spheres in viscous flow. *Intl J. Heat Mass Transfer* **27**, 1253–1262.

TAYLOR, T. D. & ACRIVOS, A. 1964 On the deformation and drag of a falling viscous drop at low Reynolds number. *J. Fluid Mech.* **18**, 466–476.

VASSEUR, P. & COX, R. G. 1977 The lateral migration of spherical particles sedimenting in a stagnant bounded fluid. *J. Fluid Mech.* **80**, 561–591.

VAN WIJNGAARDEN, L. 1976 Hydrodynamic interaction between gas bubbles in liquid. *J. Fluid Mech.* **77**, 27–44.

VAN WIJNGAARDEN, L. 1993 The mean rise velocity of pairwise-interacting bubbles in liquid. *J. Fluid Mech.* **251**, 55–78.

YUAN, H. & PROSPERETTI, A. 1994 On the in-line motion of two spherical bubbles in a viscous fluid. *J. Fluid Mech.* **278**, 325–349.

YURKOVETSKY, Y. & BRADY, J. 1995 Statistical mechanics of bubbly liquids. *Phys. Fluids* **8**, 881–895.